



Novel photosensitizer for dye-sensitized solar cell based on ionic liquid-doped blend polymer electrolyte

Dheeraj Devadiga¹ · M. Selvakumar¹ · Prakasha Shetty¹ · M. G. Mahesha² · Deepak Devadiga³ · T. N. Ahipa³ · S. Senthil Kumar⁴

Received: 30 May 2020 / Revised: 8 February 2021 / Accepted: 13 February 2021 / Published online: 2 March 2021
© The Author(s) 2021

Abstract

The existing energy situation demands not only the huge energy in a short time but also clean energy. In this regard, an integrated photo-supercapacitor device has been fabricated in which photoelectric conversion and energy storage are achieved simultaneously. A novel carbazole-based dye is synthesized and characterized for photosensitizer. The silver-doped titanium dioxide (Ag-TiO₂) is synthesized, and it is used as photoanode material. Different concentrations of tetrabutylammonium iodide (TBAI)-doped polyvinyl alcohol–polyvinylpyrrolidone (PVA-PVP) blend polymer electrolytes are prepared, and their conductivity and dielectric properties were studied. Reduced graphene oxide (r-GO) is synthesized by a one-pot synthesis method and confirmed using Raman spectroscopy for counter electrode material in dye-sensitized solar cell (DSSC) and supercapacitor electrodes. The DSSC having 4% Ag-TiO₂-based photoanode showed the highest efficiency of 1.06% (among r-GO counter electrodes) and 2.37% (among platinum counter electrodes). The supercapacitor before integration and after integration exhibits specific capacitance of 1.72 Fg⁻¹ and 1.327 Fg⁻¹, respectively.

Keywords Dye-sensitized solar cell · Supercapacitor · Silver doped titanium dioxide · Carbazole based dye · Blend polymer electrolyte · Reduced graphene oxide

Introduction

As a result of the energy crisis, demand for renewable energy resources has become critical and, in particular, the use of

solar energy is gaining supreme interest due to its abundant availability in nature [1]. Solar cells can be used to transform solar energy into electric energy. While dominant on the commercial market, the efficiency of silicon-based solar cells

Highlights

- Novel D-π-A carbazole-based dye was synthesized.
- TiO₂ and 2%, 4% and 6% Ag-doped TiO₂ were synthesized using a modified sol-gel method.
- Polyvinyl alcohol–polyvinylpyrrolidone (PVA-PVP) blend polymer electrolytes doped with different concentrations of tetrabutylammonium iodide were prepared.
- Reduced graphene oxide was synthesized from graphite by one-pot synthesis method.
- Using CaBa dye, dye-sensitized solar cells were fabricated and integrated with supercapacitor.

✉ M. Selvakumar
chemselva78@gmail.com

¹ Department of Chemistry, Manipal Institute of Technology, Manipal Academy of Higher Education, Manipal, Karnataka 576104, India

² Department of Physics, Manipal Institute of Technology, Manipal Academy of Higher Education, Manipal, Karnataka 576104, India

³ Centre for Nano and Material Sciences, Jain University, Jain Global Campus, Jakkasandra Post, Ramanagara District, Bangalore 562112, India

⁴ Electrodeposition and Electrocatalysis Division, CSIR-Central Electrochemical Research Institute, Karaikudi 630003, India

entails some environmental problems since it produces harmful chemicals such as silicon tetrachloride and trichlorosilane. Scientists have therefore focused on hybrid solar cells that are typical of low material costs and simple manufacturing processes. Presently, dye-sensitized solar cells (DSSCs) have gained considerable attention among hybrid solar cells because of their advantages like low cost of production, long life, low light performance, variety, mechanical robustness and flexible product integration [2, 3].

In the DSSC, the sensitizer plays a pivotal role because it initiates the electrical current by absorbing visible light in the solar cell [4]. Until the date, the state-of-the-art DSSCs are based on single sensitizers such as ruthenium dyes [5] and porphyrin dyes [6, 7] which have reached maximum photoconversion efficiency (PCE) under standard illumination. Metal-based sensitizers have few drawbacks for real application in DSSCs, including rareness, difficulty in purifying, environmental hazards and low molar extinction coefficients [5]. Because of their low toxicity, high structural versatility, being environmentally friendly, lower molar extinction coefficients and facile synthesis, metal-free organic sensitizers have drawn attention over metal-based organic sensitizers [4, 8].

Typically, metal-free organic sensitizers are in donor– π –acceptor structure because this structure can produce intramolecular charge transfer (ICT) from donor to acceptor, improve light-harvesting capabilities and broaden the sensitizer absorption spectrum [9]. Different chromophores with different steric and electronic characters are used as electron donors, such as carbazole [10], phenothiazine [11], coumarin [12], indoline [13] and triarylamine [14]. In order to enhance the ability of light harvesting and to help intramolecular charge transfer, π -bridges are incorporated. Among these donors, carbazole is widely used for its electron-rich properties, good hole transport capability as well as very good chemical and thermal stability [15]. Not only the donor group but also the anchoring group play an important role in the performance of the DSSC. With the help of the anchoring groups, the sensitizer covalently bonded to the TiO₂ surface shows a strong coupling and good stability of the device [16]. In most of the sensitizers, carboxylic acids (COOH) are commonly used as an acceptor unit due to their good adherence to the semiconductor layer. The electron injection is carried out through this adhesion, which is the main mechanism that begins the electrical circuit in the DSSC. The conductive band of the semiconductor is positively shifted after sensitizing adsorption due to the deprotonation of the COOH acceptor group, resulting in an open-circuit photovoltage (V_{OC}) loss [17].

Solar conversion efficiency relies on open-circuit voltage (V_{OC}), photocurrent density (J_{SC}) and fill factor (FF) of the DSSCs. The J_{SC} and FF are based on the adsorption and charge transport of dye molecules. Therefore, in order to enhance the photovoltaic properties of TiO₂, it is important to

increase its surface area, the effect of light harvesting, the adsorption activity of dye molecule and the charge transport. The doping method has been widely used to synthesize anode materials to improve the charge transfer capability and increase the V_{OC} [18]. There are many studies in which silver-doped TiO₂ was used as an anode material for DSSC applications because Ag doping increases dye adsorption and surface area and enhances interfacial charge transfer [19–21].

Liquid electrolyte-based DSSCs have many drawbacks, such as evaporation of the solvent, electrode degradation, degradation of the attached dye and difficulty in sealing the cell, which leads to lower cell life span [22]. Polymer electrolytes are used to address these drawbacks with volatile liquid electrolytes. It increases the long-term reliability of DSSCs and reduces issues such as sealing, electrode corrosion and leaking [23]. Some of the ion salts widely used in electrolytes are quaternary ammonium salts. The quaternary ammonium salts also produce cations instead of iodide ions. Reports show that cations have an effect on the transport rate, the strength of the sensitizing surface attachment and the oxidation rate of iodide that may affect the performance of solar cells [24].

In DSSCs, the counter electrode also plays a vital role in collecting electrons from the external circuit and transfers them to the cell, transmitting unabsorbed light back to the cell, which increases the use of sunlight. Most materials are used as counter electrodes, such as metal counter electrodes, carbon counter electrodes, polymer counter electrodes and hybrid counter electrodes [25]. Carbon-based materials such as graphene sheets, amorphous carbon and carbon nanotubes have favourable properties as Pt-free counter electrodes. Graphene is best known, among other carbon materials, for its excellent mechanical, optical, thermal and electrical properties [26–28].

The electrical energy generated in DSSC from sunlight cannot be stored directly. Henceforth, there is a demand for emergence of suitable energy storage technologies. The lightweight, small-sized, high-reliable and high-power density energy systems can be obtained by operating integrated power pack, energy harvesting and storage technologies together. In this regard, the development of integrated energy harvesting and storage technologies is required, which captures sunlight and converts into solar energy and simultaneously stores electrical energy. In recent years, the solar rechargeable supercapacitors (SCs) have been developed for the effective use of solar energy by integrating the solar cells and SCs [29].

In this work, we synthesized novel carbazole-based dye for photosensitizer and prepared different concentrations of Ag-doped TiO₂ nanoparticles for photoanode. The reduced graphene oxide was prepared for counter electrode and tetrabutylammonium iodide (TBAI) ionic liquid-doped polyvinyl alcohol–polyvinylpyrrolidone (PVA-PVP) blend polymer electrolyte used for the fabrication of hybrid supercapacitor. The integrated hybrid device structure is shown in Fig. 1.

Experimental

Materials and methods of preparation

All chemicals and reagents were purchased from Merck, TCI and Sigma-Aldrich and used without any further purification. The FTIR spectra are recorded in KBr pellet using a Shimadzu 8400S spectrometer in the range 400–4000 cm^{-1} . $^1\text{H-NMR}$ and $^{13}\text{C-NMR}$ spectra are recorded in Bruker (400 MHz and 100 MHz, respectively) spectrometers with TMS as an internal reference. The X-ray diffraction (XRD) was recorded in Bruker Miniflex 600 model. All the electrochemical measurements were carried out using BioLogic SP-150. The I - V characterizations of fabricated DSSCs were carried out using a Keithley 2450 source meter.

Synthesis of substituted 4-(3-(9-ethyl-9H-carbazol-3-yl)acryloyl)benzoic acid

Ethyl-9H-carbazole-3-carbaldehyde (1 equivalent) was added to the stirred mixture of 4-acetylbenzoic acid (1 equivalent) in ethanol, followed by 10% NaOH. The reaction mixture was agitated for 24 h at room temperature (RT) (Scheme 1). The precipitate obtained was filtered, washed with water and ethanol, dried and recrystallized using methanol to afford the desired product with 77% yield. M.P. = 220 °C, FTIR (cm^{-1}): 1581.08 (C=C), 1654.42 (–C=C–C=O), 1681.29 (–C=O), 2984.4 (CH), 3454.33 (OH); $^1\text{H NMR}$ (DMSO) δ (ppm): 1.35 (t, $J = 7.1$ Hz, 3H), 4.50 (q, $J = 7.1$ Hz, 2H), 7.29 (t, $J = 7.5$ Hz, 1H), 7.52 (t, $J = 7.7$ Hz, 1H), 7.69 (dd, $J = 16.2, 8.4$ Hz, 2H), 8.03 (d, $J = 22.5$ Hz, 3H), 8.12 (d, $J = 8.1$ Hz, 2H), 8.26 (dd, $J = 12.5, 7.9$ Hz, 3H), 8.78 (s, 1H); $^{13}\text{C NMR}$ (DMSO) δ (ppm): 14.24, 37.69, 110.08 (2C), 119.20, 120.07, 121.14, 122.69, 122.75, 123.19, 126.04 (2C), 126.67, 127.67, 128.74 (2C), 129.92 (2C), 140.59, 140.91, 141.67,

146.81, 167.75, 189.21; ESI-MS (m/z): $[\text{M}]^+$ calculated for $\text{C}_{24}\text{H}_{19}\text{NO}_3$:369.42, found: 370.0244.

Synthesis of pristine and silver-doped titanium dioxide

TiO_2 and silver-doped titanium dioxide (Ag- TiO_2) nanoparticles were synthesized by a modified sol-gel route [30]. The procedures are as follows: to the stirred solution of acetic acid, titanium tetraisopropoxide (TTIP) was added followed by slow addition of water. (The TTIP, acetic acid and water are taken in 0.1:1:10 molar ratios). Then, the mixture was agitated for 6 h to achieve a clear translucent solution and it was finally dried at 90 °C. The dried sample was calcinated for 2 h at 600 °C. In order to prepare Ag- TiO_2 , silver nitrate (2 mol%, 4 mol% and 6 mol%) in water was added to the mixture of titanium isopropoxide.

Preparation of PVA-PVP blend polymer electrolytes

PVA and PVP (1:1) are dispersed in DMSO under continuous stirring. After homogeneous solution formation, different weight percentages (10 to 50 wt%) of TBAI was added followed by the addition of I_2 into the polymer solution (one-tenth of the molar ratio of TBAI). The mixture was stirred until the solution become homogenous. The resultant polymer solution was poured over a Petri dish (Teflon) and dried overnight at 90 °C in a vacuum oven to aid in the evaporation of solvents.

Preparation of reduced graphene oxide

A mixture of 13.3 mL of H_3PO_4 and 120 mL of concentrated H_2SO_4 (1:9 ratio) was added slowly to a mixture of 6 g of KMnO_4 and 1 g graphite powder (6:1 weight equivalent). The mixture was then agitated for 24 h at 120 °C. Then, it was

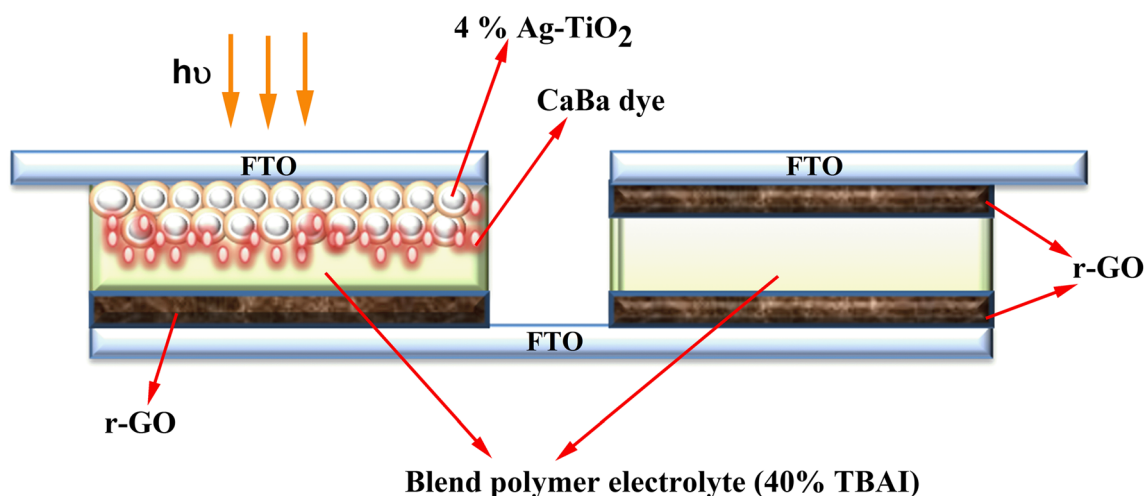
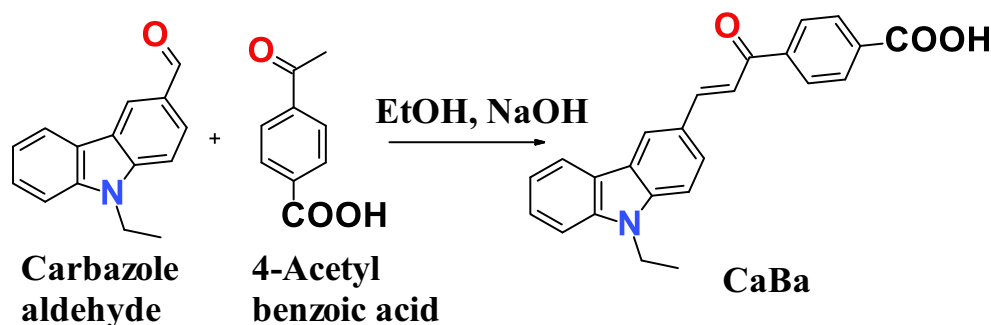


Fig. 1 Schematic illustration of an integrated device (DSSC-SC)

Scheme 1 Synthesis of CaBa dye



cooled to RT and poured into ice with 2 mL 30% H_2O_2 . A black precipitate with a clear supernatant solution was obtained [31]. The precipitate was purified by water washing in continuous ultracentrifugation followed by vacuum filtration. To extract excess water from the samples and ensure fast drying at RT, acetone has been added to the sample. After drying, solid samples were made ready for characterization.

Fabrication of DSSC

Fluorine-doped tin oxide (FTO)-coated glass substrates were cleaned using detergent, water, acetone and isopropyl alcohol, respectively. After cleaning, substrates were immersed in 40 mM titanium tetrachloride for 45 min at 70 °C to form a blocking layer. The TiO_2 or Ag- TiO_2 layer was coated by doctor blade technique using water, acetyl acetone and hydroxypropyl cellulose mixture. The substrates were then placed for sintering for 30 min at 450 °C. Then, substrates were dipped in 0.5 mM methanol solution of synthesized 4-(3-(9-ethyl-9H-carbazol-3-yl)acryloyl)benzoic acid (CaBa) dye for 24 h at RT. Counter electrodes were prepared by coating prepared reduced graphene oxide (r-GO) on the FTO substrate. Then, prepared high conductive blend polymer electrolyte was sandwiched between two electrodes.

Fabrication of SC-integrated DSSC

The integrated device was fabricated as shown in Fig. 1. On the common platform of r-GO, counter electrode in SC cell was fabricated using r-GO as positive and negative electrodes with prepared blend polymer electrolyte film sandwiched between them.

Characterization techniques

TiO_2 and 4% Ag- TiO_2 were coated on FTO substrate to measure cyclic voltammograms (CVs) of the material. CV was recorded in a three-electrode system having an aqueous 0.5 M KOH solution. To investigate electrochemical impedance spectroscopy (EIS) and the Tafel polarization curve, the dummy cells were fabricated with two identical electrodes having TiO_2 or 4% Ag- TiO_2 material and separated by 40%

TBAI electrolyte film. The EIS measurements were carried out within the frequency of 100 mHz–1 MHz. Different concentrations of TBAI-doped blend polymer electrolyte film were placed between the copper electrodes having an area of 1 cm^2 . Paper clips were used for good connectivity between the electrodes and electrolyte. The conductivity, impedance and dielectric characteristics have been studied using EIS. The measurements of the EIS were carried out at 100 mHz–1 MHz frequency. r-GO and Pt were coated on FTO substrate to measure the CV of the material. CV was recorded in a three-electrode system having a liquid electrolyte (KI and I_2 in acetonitrile). To investigate EIS, the dummy cells were fabricated having two r-GO or Pt identical electrodes and separated by 40% TBAI electrolyte film and experiments were carried out within the frequency of 100 mHz–1 MHz. Further, the Tafel polarization curves were also analysed using the symmetric cells. The I – V characterizations of fabricated DSSCs were carried out under air mass (AM) 1.5 condition using Keithley 2450 source meter, and EIS measurements of fabricated devices were carried out at 100 mHz–1 MHz frequency.

Results and discussion

Optical properties of CaBa

The ultraviolet–visible (UV–vis) absorption spectrum of a CaBa dye in tetrahydrofuran (THF) solution is shown in Fig. 2a. The CaBa dye shows three distinct bands of absorption: one band at 289.6 nm corresponding to the π – π^* electron transitions of the conjugated molecules, the another band at 394 nm which can be attributed to an ICT between the carbazole-donating unit with the anchor group and the third band which is in between these two bands which arises due to the highest occupied molecular orbital (HOMO) $-1 \rightarrow$ lowest unoccupied molecular orbital (LUMO) or HOMO \rightarrow LUMO $+1$ transition [32].

The UV–vis spectrum of CaBa dye-coated TiO_2 is displayed in Fig. 2b in which broadened absorption of CaBa dye was observed after anchoring to the TiO_2 surface and the onset of absorption got redshifted to more than 30 nm. This is because of the deprotonation of the acid group present in

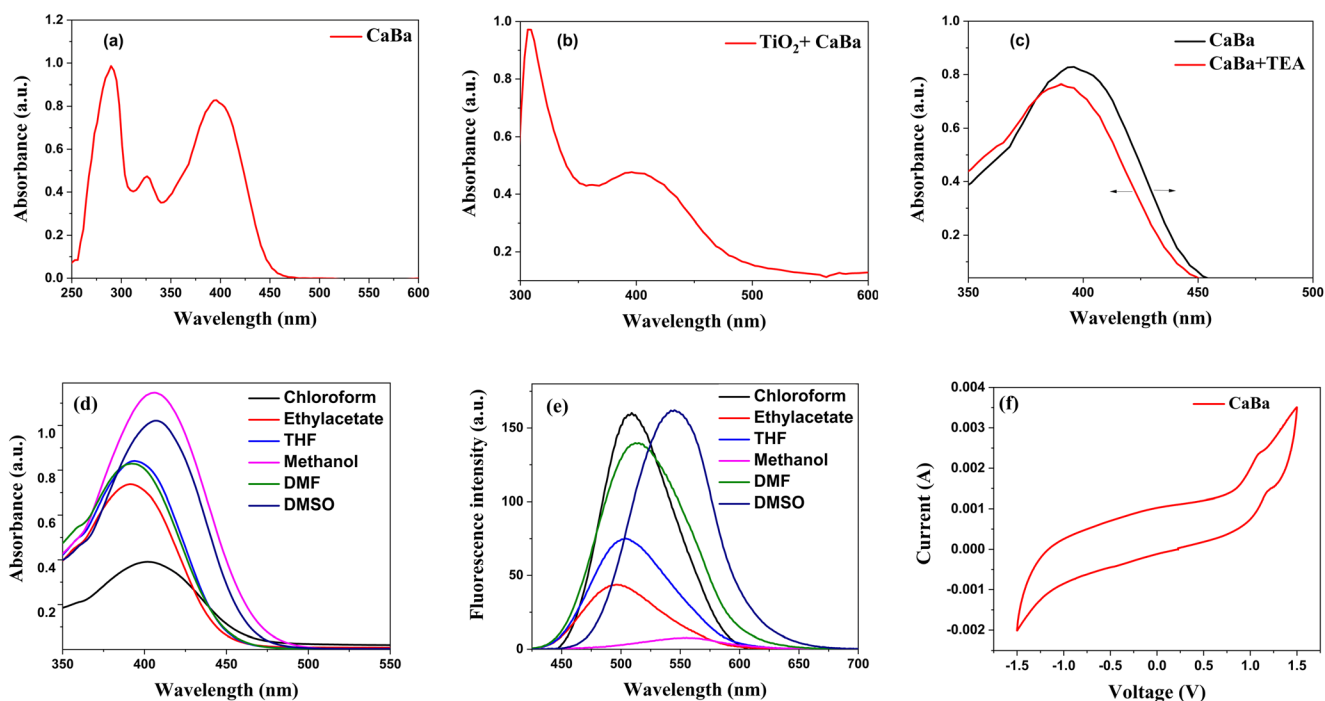


Fig. 2 **a** UV–visible spectra of CaBa dye in THF (10^{-5} M). **b** UV–visible spectra of CaBa dye coated on TiO_2 film. **c** UV–visible spectra of CaBa dye in THF in the presence of TEA. **d** UV–visible spectra of CaBa dye in

different solvents. **e** Fluorescence spectra of CaBa dye in different solvents. **f** Cyclic voltammogram of CaBa dye

CaBa dye and the charge transfer (CT) transitions of the CaBa dye anchored on TiO_2 . The UV–vis spectra of CaBa dye taken in THF solvent in the presence of triethylamine (TEA) to understand CT transitions are shown in Fig. 2c. Due to the deprotonation, CaBa dye showed blueshift and it suggests in the presence of TEA, acceptor capacity was reduced, whereas the redshift in the absorption spectra of the CaBa dye-bound TiO_2 film suggests the *J*-aggregation of a dye [33]. Aggregation usually results in a loss of exciton due to recombination, but many literature studies also suggest the effect of *J*-aggregation which contributes to better light-harvesting capacity which, in turn, leads to enhanced device efficiency [1, 34, 35].

Effect of solvents on absorption and emission spectra of CaBa dye

The absorption and emission spectra of CaBa dye were measured at 1×10^{-5} M concentration in different solvents with different polarity levels, and obtained results are depicted in Fig. 2d and e. Figure S5 depicts the solvent effect on CaBa dye under visible light (normal light), short UV and long UV illumination. The CaBa dye exhibited a broad absorption band, suggesting that the allowed transition of π – π^* with charge transfer character [36]. The calculated values of absorption maximum, emission maximum, optical band gap and CIE coordinates of CaBa dye in different solvents are given in Table S1. Absorption spectra of CaBa dye showed

a minimal difference in absorption maxima going from non-polar solvents to polar solvents. A redshift of 16 nm was seen in the absorption maxima of CaBa dye going from non-polar solvents to polar solvents. The emission spectra of CaBa dye in different solvents were recorded under their respective excitation wavelengths, and obtained spectra are shown in Fig. 2e. The CaBa dye showed different emission bands as the polarity changes (496 to 555 nm). The emission spectrum was not much changed in aprotic solvents except DMSO due to its high dielectric constant/high polarity of the solvent; however a significant redshift of 59 nm is seen in protic solvent (i.e. methanol solvent), which can be attributed to the hydrogen bond formation between the acid functionality of the dye CaBa and the solvent. This result suggests that involvement of photo-induced ICT in the singlet-excited state from the electron-donating to electron-accepting group with larger dipole moment in the excited state than in the ground state [37]. The fluorescence intensity of CaBa dye in methanol was comparatively of lesser intensity when compared to the intensities of CaBa dye in aprotic polar solvents. The reason for these different solvent effects on fluorescence intensity may be due to the effect of hydrogen bond on the radiationless deactivation process [38]. Further, luminance parameters of CaBa dye in different solvents were characterized by the CIE system with two colour coordinates (*x* and *y*) under long UV illumination. From the CIE coordinate diagram (Fig. S6), it is noted that, when the dye CaBa is dissolved in solvents such as chloroform, ethyl acetate, THF and DMF, it emits the

colour in bluish green region under long UV illumination, whereas, when it is dissolved in the highly polar DMSO and protic methanol solvents, it exhibits the colour in the greenish yellow region under long UV illumination.

Electrochemical properties of CaBa dye

To determine electrode potential and HOMO and LUMO energy levels of CaBa dye, cyclic voltammetry (CV) was performed in acetonitrile solution containing 0.1 N TEABF₄ at a scan rate of 20 mV s⁻¹. These values are useful to determine the thermodynamic feasibility of electron injection from the HOMO level of dye molecule into the metal oxide conduction band and electrolyte dye regeneration. Figure 2f depicts the cyclic voltammogram of CaBa dye. CaBa dye showed first oxidation potential corresponding to HOMO versus NHE at 1.08 V (Table 1) which is more positive than the redox potential of iodine/iodide electrolyte (~0.4 V vs. NHE), indicating the regeneration of the oxidized dye ground state by accepting an electron from electrolyte [39]. The excited-state oxidation potential, i.e. LUMO energy level of the dye, was calculated from the equation $E_{LUMO} = E_{HOMO} - E_{0-0}$ and was found to be -1.69 V versus NHE. The LUMO is more negative than the conduction band of TiO₂ (-0.5 V vs. NHE), and it indicates that injection of photogenerated electrons into the conduction band of TiO₂ is energetically permitted [40]. From these values, we can evidently deduce that CaBa dye could be used as a sensitizer in DSSC.

XRD analysis of TiO₂ and Ag-doped TiO₂

The XRD patterns of synthesized TiO₂ and Ag-TiO₂ nanoparticles are shown in Fig. 3. All the diffraction peaks of the TiO₂ and Ag-TiO₂ nanoparticles could be indexed to the anatase crystalline phase of TiO₂ (space group I41/amd, card no. 21-1276 in the JCPDS database). The intense and sharp peaks near 25.4°, 37.9°, 48.1° and 54° correspond to diffraction planes such as (101), (004), (200) and (211), respectively.

Table 1 Photophysical properties of CaBa dye

Abs. λ_{max} ^a (nm)	λ_{max}/TiO_2 ^b (nm)	λ_{int} ^c (nm)	HOMO ^d (vs. NHE) (V)	E_{0-0} ^e (eV)	LUMO ^f (vs. NHE) (V)
289.6	401.6	447	1.08	2.77	-1.69
326					
394					

^a Absorptions measured in THF

^b Maximum absorption on TiO₂ film

^c $\lambda_{intersection}$

^d HOMO of dyes measured by cyclic voltammetry in 0.1 N tetraethylammonium tetrafluoroborate (TEABF₄) in acetonitrile

^e $E_{0-0} = \frac{1240}{\lambda_{int}}$

^f $E_{LUMO} = E_{HOMO} - E_{0-0}$

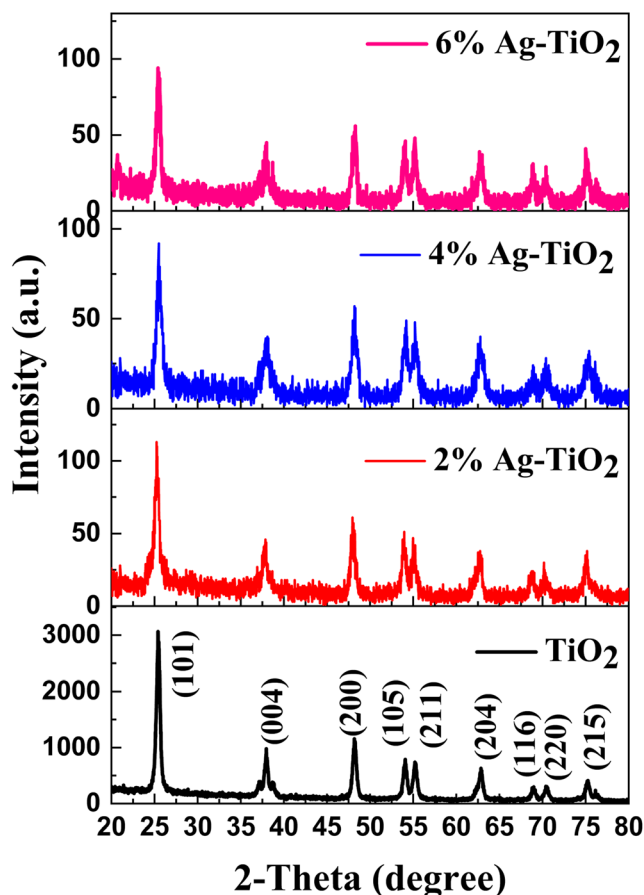


Fig. 3 XRD patterns of TiO₂ and Ag-TiO₂ nanoparticles

The crystallite size of pristine TiO₂ and 2%, 4% and 6% Ag-doped TiO₂ was calculated to be 17.1 nm, 15 nm, 10.8 nm and 15.9 nm, respectively, by the Debye Scherer equation. It is observed that as the Ag addition increases, the particle size reduces till optimum point then increases. There are no peaks related to Ag in XRD data, even for 6% Ag-TiO₂, which suggests dopants are highly dispersed in the TiO₂ samples [41]. For the Ag-TiO₂ nanoparticles, the (101) peak intensity was less compared to bare TiO₂ nanoparticles. It should be noted that at low Ag contents, doping did not affect the

anatase crystalline phase; however, it affected the crystallinity of the product. Ag^+ or Ag^{2+} ions are introduced into the periodic TiO_2 crystal lattice by causing strain into the system, and as a consequence, the lattice periodicity is altered and the crystal symmetry decreases [18].

Morphology and structures of TiO_2 and 4% Ag-TiO_2

High-resolution transmission electron microscopy (HRTEM) images of TiO_2 and 4% Ag-TiO_2 are displayed in Fig. 4a and b and d and e, respectively, and its selected area electron diffraction (SAED) patterns are displayed in Fig. 4c and f, respectively. TiO_2 and 4% Ag-TiO_2 displayed almost spherical shaped particles with an average particle size of 17 nm and 11 nm, respectively, which is in close agreement with the crystallite size obtained from the XRD. Interplanar spacing of $d = 0.359$ nm was displayed by TiO_2 nanoparticles which is corresponding to the (101) plane of anatase TiO_2 [42, 43]. On the other hand, interplanar spacing of $d = 0.25$ nm was displayed by 4% Ag-TiO_2 nanoparticles which is corresponding to the (002) plane of Ag_2O [44]. This confirms that Ag was effectively doped into the TiO_2 [18, 45]. The anatase phase of both samples is further confirmed by SAED pattern [46]. In addition, EDAX spectrum (Fig. 5e) and mapping of elements (Fig. 5a–d) of 4% Ag-doped TiO_2 indicate that Ag was successfully doped to the TiO_2 .

Electrochemical performance of TiO_2 and 4% Ag-TiO_2

Figure 6a displays the CV of TiO_2 and 4% Ag-TiO_2 recorded in an aqueous 0.5 M KOH solution, with a Pt counter electrode (CE) and an Ag/AgCl as the reference electrode. There is no measurable reduction or oxidation peak obtained for bare TiO_2 within the potential scan range between -0.5 and 0.5 V. But in the case 4% Ag-doped electrode, the anodic (1 and 2) and cathodic (3 and 4) peaks were observed for TiO_2 nanoparticle electrode which is attributed to the oxidation of Ag (1 [$\text{Ag/Ag}_2\text{O}$] and 2 [$\text{Ag}_2\text{O/AgO}$]) and the reduction of silver oxide (3 [$\text{AgO/Ag}_2\text{O}$] and 4 [$\text{Ag}_2\text{O/Ag}$]) [47–50].

To analyse the charge transfer kinetic property of TiO_2 and 4% Ag-TiO_2 nanoparticles, the EIS investigation was carried out under dark condition using the dummy cells. Dummy cells were fabricated with two identical electrodes and separated by electrolyte film. Figure 6b shows the Nyquist plots of TiO_2 and 4% Ag-TiO_2 nanoparticles. It can be seen from Fig. 6b that the grain boundary resistance of 4% Ag-TiO_2 is lower than that of TiO_2 which confirms the improvement in conducting behaviour of 4% Ag-TiO_2 . The doping of the Ag metal ion into the TiO_2 matrix enhances the mobility of the prepared material and raises the charge carrier, confirming the fastest interfacial electron transfer and the lowest recombination rate within composite samples [51, 52].

Tafel plots of 4% Ag-doped and bare TiO_2 are shown in Fig. 6c. The disparity in curve behaviour can be attributed to

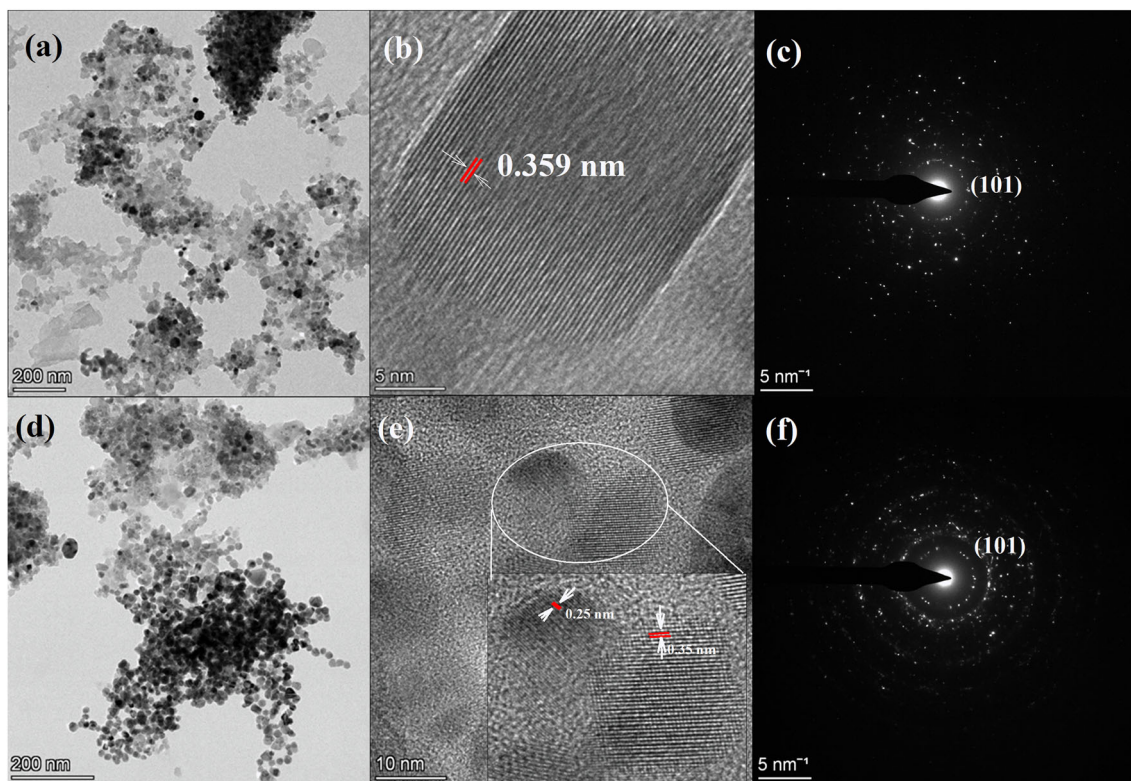


Fig. 4 HRTEM images of TiO_2 (a, b) and 4% Ag-TiO_2 (d, e) and SAED patterns of TiO_2 (c) and 4% Ag-TiO_2 (f)

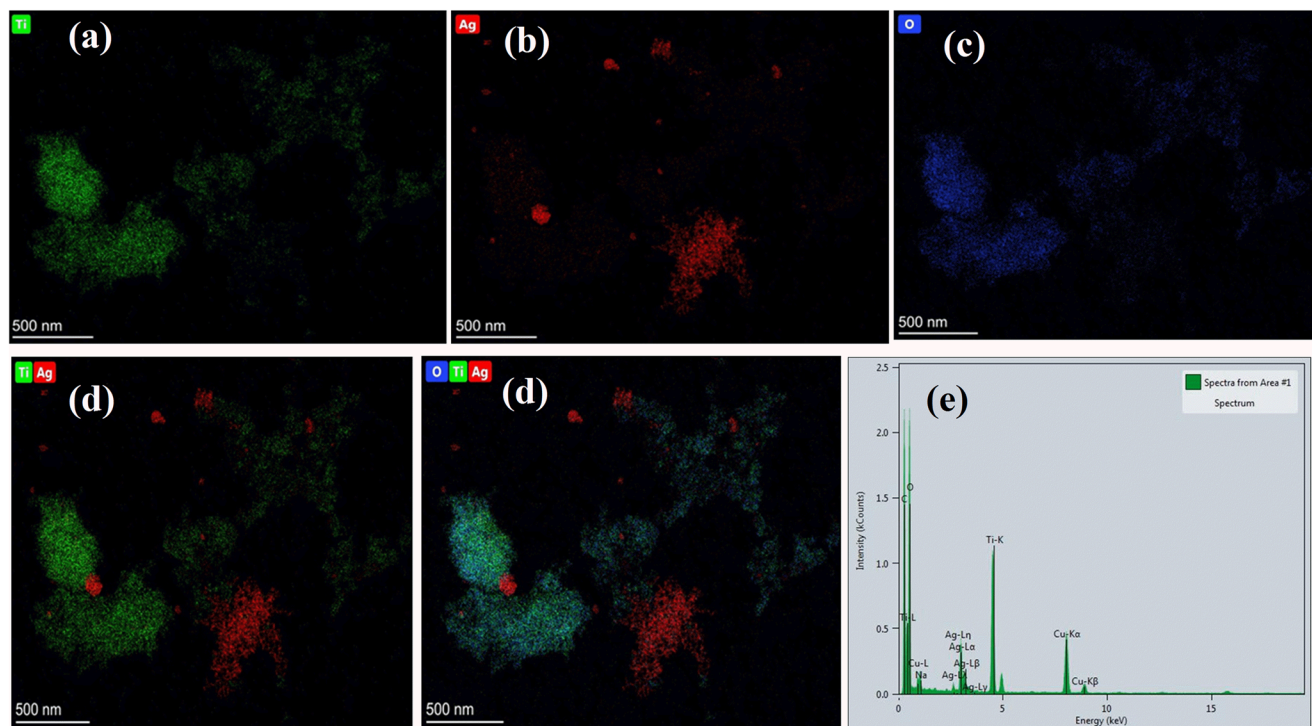


Fig. 5 Mapping of elements (a–d) and EDAX spectra (e) of 4% Ag-TiO₂

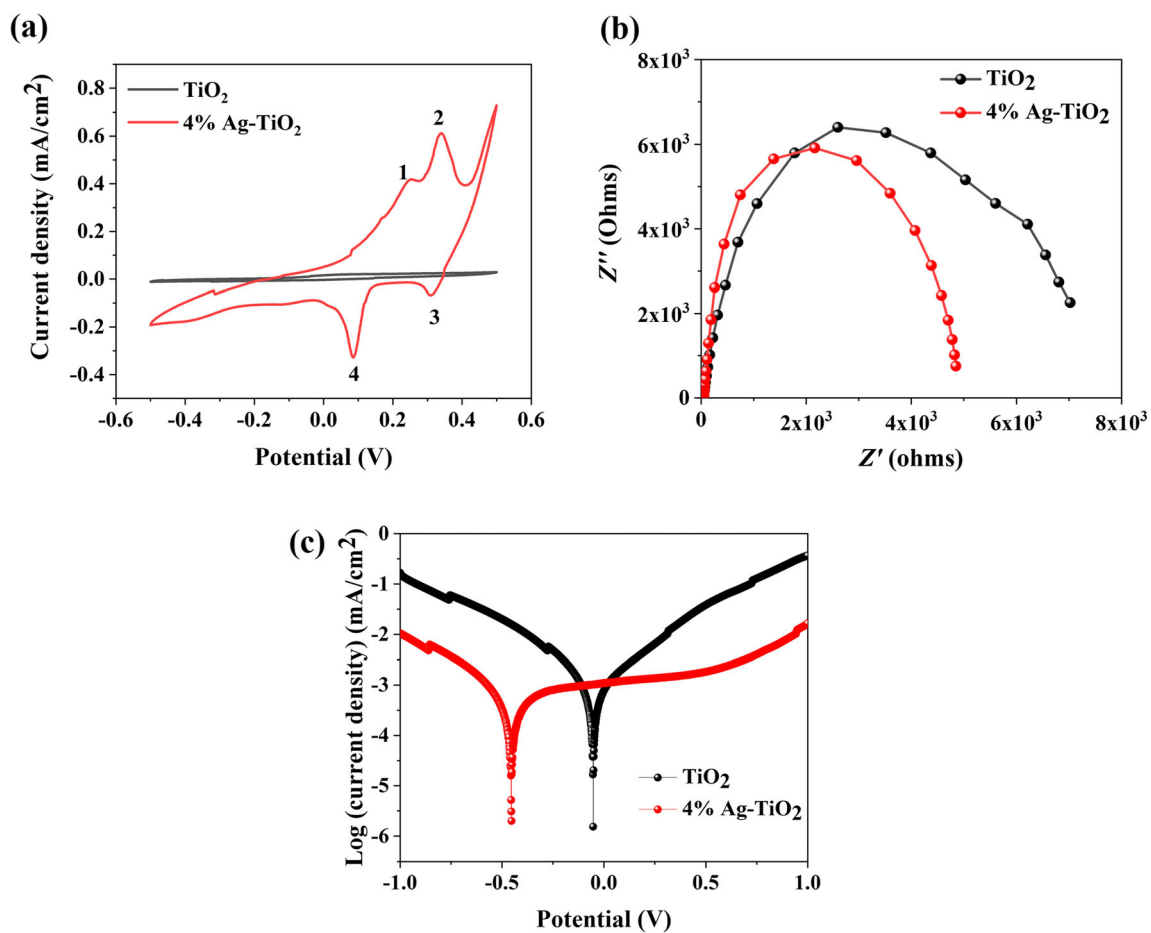


Fig. 6 a CV, b EIS and c Tafel plots of TiO₂ and 4% Ag-TiO₂

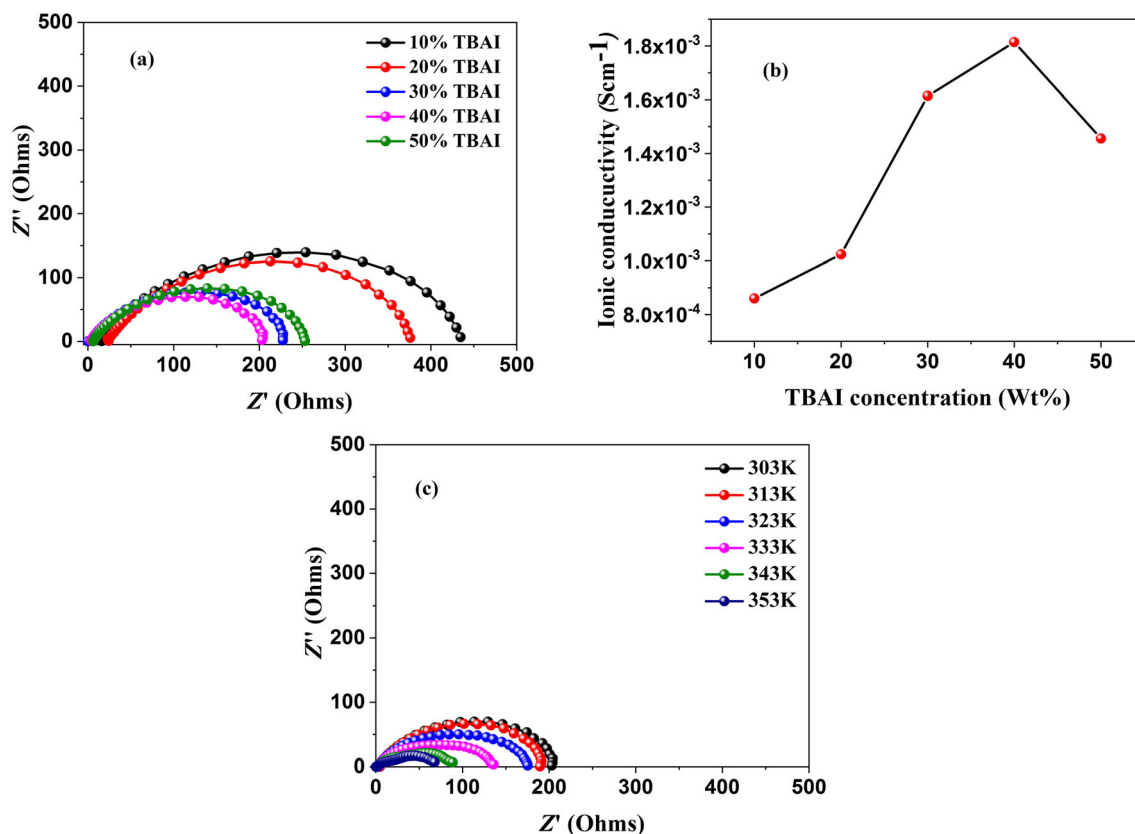


Fig. 7 a Complex impedance plots of BPE samples with different TBAI concentrations at room temperature. b Ionic conductivity of BPE samples. c Complex impedance plots of 40% TBAI sample at different temperatures

different processes of charge transfer at the interface of the photoanode. The charge will first fill the empty surface states below the conduction band edge with a negative bias applied to a semiconductor electrode and then accumulate in the space charge layer [53]. In contrast to the TiO_2 , the polarization curve of 4% Ag- TiO_2 showed a negative shift, which implies the negative shift of TiO_2 's flat band potential (E_{fb}) after Ag doping. It is well known that V_{OC} is determined by the electrolyte's redox potential and the electrode's E_{fb} ; the E_{fb} change means the device's V_{OC} variation. A negative E_{fb} shift means a shift away from the redox potential and hence a rise in V_{OC} [54, 55].

Ionic conductivity studies of polymer electrolytes

The bulk resistance of the prepared polymer electrolyte was obtained from complex impedance plots ($-Z''$ vs. Z'). Polymer electrolytes with 5 different TBAI ratios are illustrated in Fig. 7a. It was observed that the conductivity of blend polymer electrolytes (BPE) increases with the amount of TBAI till optimum point and then decreases. Among 5 different BPEs, 40% TBAI showed the maximum conductivity as shown in Fig. 7b. Mobility of free ions and charge density influence the conductivity of polymer electrolytes. By adding more salts, the number of free ion density charges can be promoted. However, if there is excess of free ions present in polymer electrolytes, they may

have a tendency to form an aggregation of ions and pairings of ions. This phenomenon hindered the mobility of mobile charge carriers within the polymer matrix and therefore decreased ion conductivity [56]. The ionic conductivity studies of 40% TBAI BPE in the temperature range 303 to 353 K are shown in Fig. 7c. It was observed that, as the temperature increases, the conductivity also increases. As the temperature increases, the free ions acquire more kinetic energy and move more quickly; this phenomenon causes an increase in conductivity.

Dielectric behaviour of polymer electrolyte

Dielectric behaviour of polymer electrolytes can be explained using electrical and permittivity studies. Dielectric constant or real part (\mathcal{E}') and dielectric loss or imaginary part (\mathcal{E}'') are two complex dielectric parameters of permittivity dielectric studies. The variation of dielectric constant for all BPE samples with frequency is shown in Fig. S7(a). It was seen that at lower frequency, the dielectric constant for each sample is very large, and at the higher frequency, it decreases. At lower frequency, the mobile ions move around in the polymer matrixes under electric field and form a hetero-charge layer at electrode–electrolyte interface due to the accumulation of mobile ions at the interface which the layer will shield the external electrical field and later also led to the high value of the

dielectric constant [24]. At the same time, mobile ions are hardly able to be aligned to the direction of the applied field at higher frequencies and this gives rise to a very fast periodic reversal of the electric field that there is no time for the charge to build up at the interface. Hence, the polarization due to the charge accumulation decreases, leading to a decrease in a dielectric constant [57, 58]. The dielectric constant at different temperatures for the 40% TBAI sample is shown in Fig. S7(b). From the graph, it can be understood that as the temperature increases, there is rise in the dielectric constant. At higher temperature, free ions move faster due to gaining of more kinetic energy. Hence, the ability of free ions to rotate and align with the externally applied fields leads to an increase in the dielectric constant. The frequency dependence of dielectric loss for all BPE samples is shown in Fig. S7(c). It was seen that the dielectric loss for each sample approaches zero and is very large at higher and lower frequency, respectively. Nevertheless, there is a complex molecular relaxation process as variations of points are present in the graph. The dielectric loss behaviour of a 40% TBAI sample at different temperatures is summarized in Fig. S7(d). The dielectric loss is

following the trend of temperature. This can be explained by the facts that an increase in the rate of ion migration at high temperatures leads to an increase in the dielectric loss [23].

Electrical modulus studies were conducted to understand more about the relaxation behaviour of a polymer electrolyte. Figure S8(a) displays the real part modulus (M') against frequency. At the higher-frequency region, dispersion of real part modulus takes place, and when it reaches lower frequency, it approaches zero. This actually indicates that at the electrode–electrolyte interface, the occurrence of masking the electrode polarization effect can be observed. At the high-frequency region, resonance peaks are seen which indicate the samples are good ionic with a long range of conductivity relaxation [59]. Figure S8(b) displays the temperature dependence real modulus behaviour of 40% TBAI. It shows at low frequency, M' is very close to zero and, at the higher frequency, it disperses. The graph of imaginary part modulus (M'') against frequency is presented in Fig. S8(c). The graph displays M'' dispersion at high frequency, and at the lower frequency, it approaches zero. The resonance peaks are not observed in the graph, but it may appear at higher frequency. The temperature

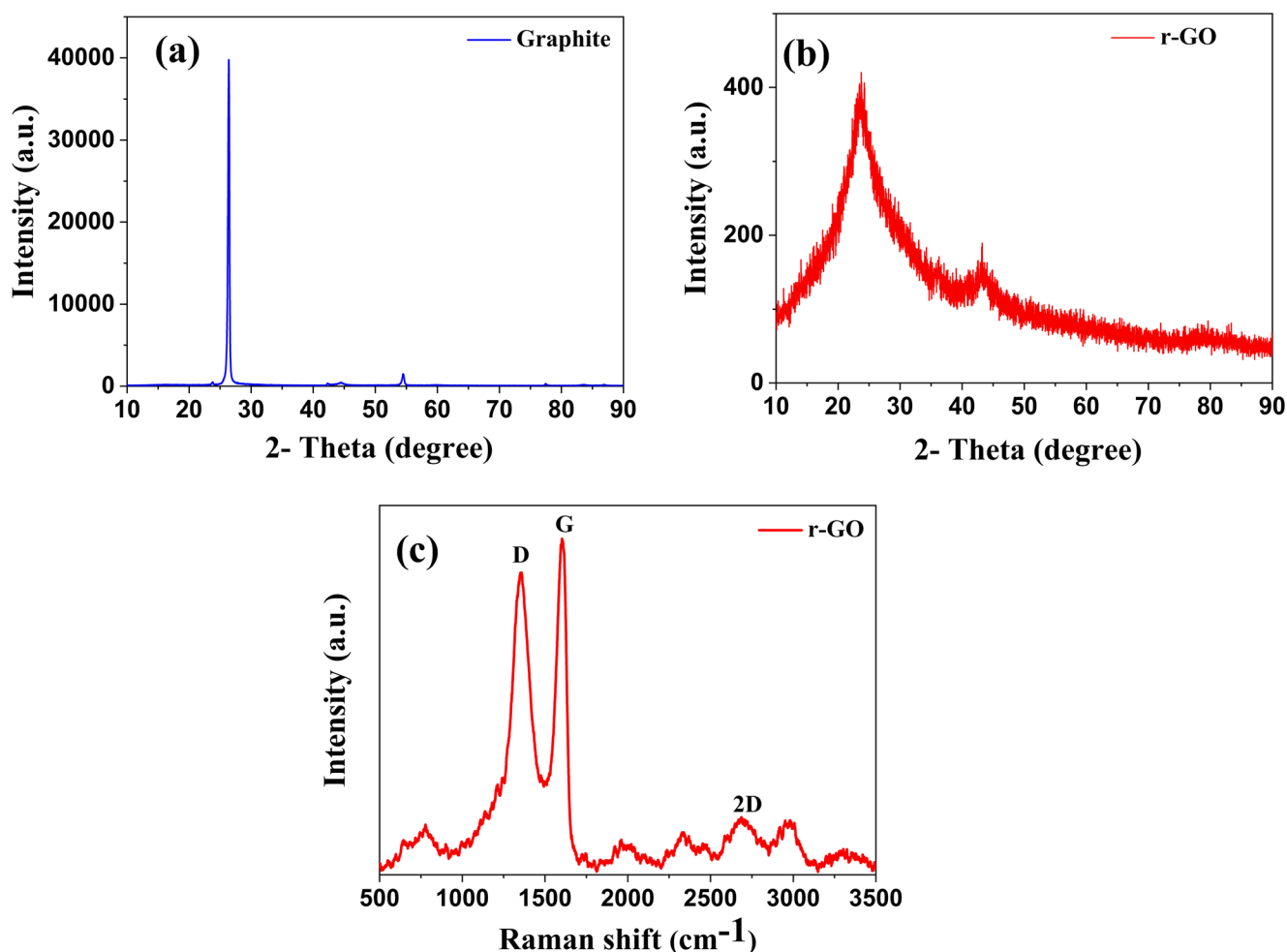


Fig. 8 a XRD spectra of graphite. b XRD spectra of r-GO. c Raman spectra of r-GO

dependence imaginary part modulus of the 40% TBAI sample is exhibited in Fig. S8(d). It shows that the peaks were shifted towards high-frequency state which indicates the values of M'' are inversely proportional to temperature. Thus, it can be concluded that at the higher temperature, the relaxation time of the samples is shorter and it is thermally activated with the hopping of free ions [60].

XRD and Raman spectra of r-GO

Figure 8a and b shows the XRD pattern of graphite and r-GO, respectively. The XRD spectra of graphite showed an intense sharp peak at 26.4° (interlayer spacing = 0.34 nm) corresponding to the distinctive feature of graphite with the hkl parameter (002) [31]. In the XRD pattern of r-GO, the existence of a broad peak at 24.3° suggests that the graphite was fully converted to r-GO. The broadening of the XRD graphene peak (002) was due to misalignments and faults in carbon sheet stacks with a larger carbon interlayer spacing [61].

Raman spectroscopy was carried out to characterize r-GO which is shown in Fig. 8c. It revealed D band and G band at 1358.5 cm^{-1} and 1602.86 cm^{-1} , respectively. The D band was observed due to the defects of C=C in the r-GO, and the G band was observed due to the in-plane vibration of C–C. The intensity ratio of D and G bands demonstrates the quality of the r-GO. The I_D/I_G value of r-GO is 0.8475. However, the prominent D peak in r-GO suggests that certain structural defects such as vacancies and topological defects still exists after the reaction [62]. The spectra also showed a 2D peak at 2686.57 cm^{-1} which indicates the number of layers in graphene. The 2D band was found to be broadened, due to the fact that the prepared graphene comprises few layers with certain defects [63]. The results obtained for r-GO by various research groups using different methods matched the results obtained in the present work [64–66].

Morphological study of r-GO

Figure 9a and b shows the HRTEM image of r-GO and its corresponding high-magnification image, respectively, and indicates the less wrinkled morphology with crystalline nature. The SAED pattern (Fig. 9c) showed strong diffraction spots with six-fold rotational symmetry with the outer spots corresponding to the (110) planes (d -spacing = 0.119 nm) and the innermost diffraction spots corresponding to the (100) planes (d -spacing = 0.201 nm), which clearly indicates the graphitic crystalline structure [67].

Electrochemical performance of r-GO and Pt

To examine the catalytic activity and reaction kinetics of the Pt and r-GO CEs, CV was carried out using a three-electrode system in liquid electrolyte. Two redox peaks were noticed at higher and lower potentials in the CV graphs of Pt and r-GO CEs (Fig. 10a) which are attributed to the reaction of $2I_3^- \rightarrow 3I_2 + 2e^-$ and $3I^- \rightarrow I_3^- + 2e^-$, respectively [68, 69]. Two parameters, the peak-to-peak separation (E_{pp}) and the peak current, represent the catalytic activity of CEs [70]. A smaller E_{pp} implies greater reversibility of the redox reaction, and a faster reduction rate is demonstrated by a higher cathodic peak current density [71, 72]. From Fig. 10a, we can notice that the E_{pp} values for the Pt CE were lower compared to those for the r-GO CE and the cathodic peak current density for the Pt CE is higher compared to that for r-GO. The lower E_{pp} and higher peak current density of Pt CE indicate good electroreductive behaviour to I^-/I_3^- redox. These findings are in agreement with EIS experiment and DSSC with high efficiency.

EIS experiment was carried out using symmetric cells to further verify the electrocatalytic abilities of r-GO and Pt CEs. Figure 10b shows the EIS spectra of r-GO and Pt CEs with the equivalent circuit model in the inset. According to the

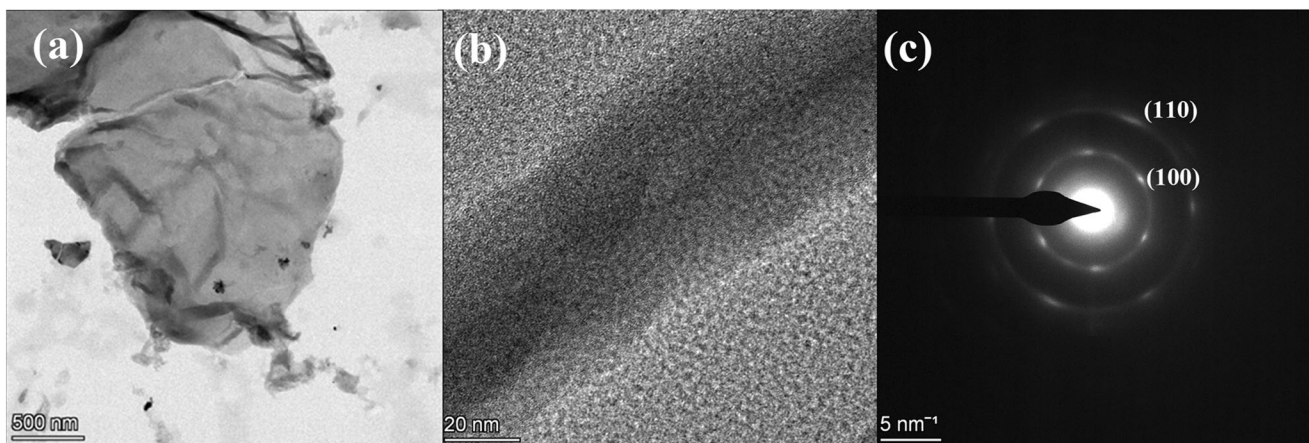


Fig. 9 HRTEM images (a, b) and SAED pattern (c) of r-GO

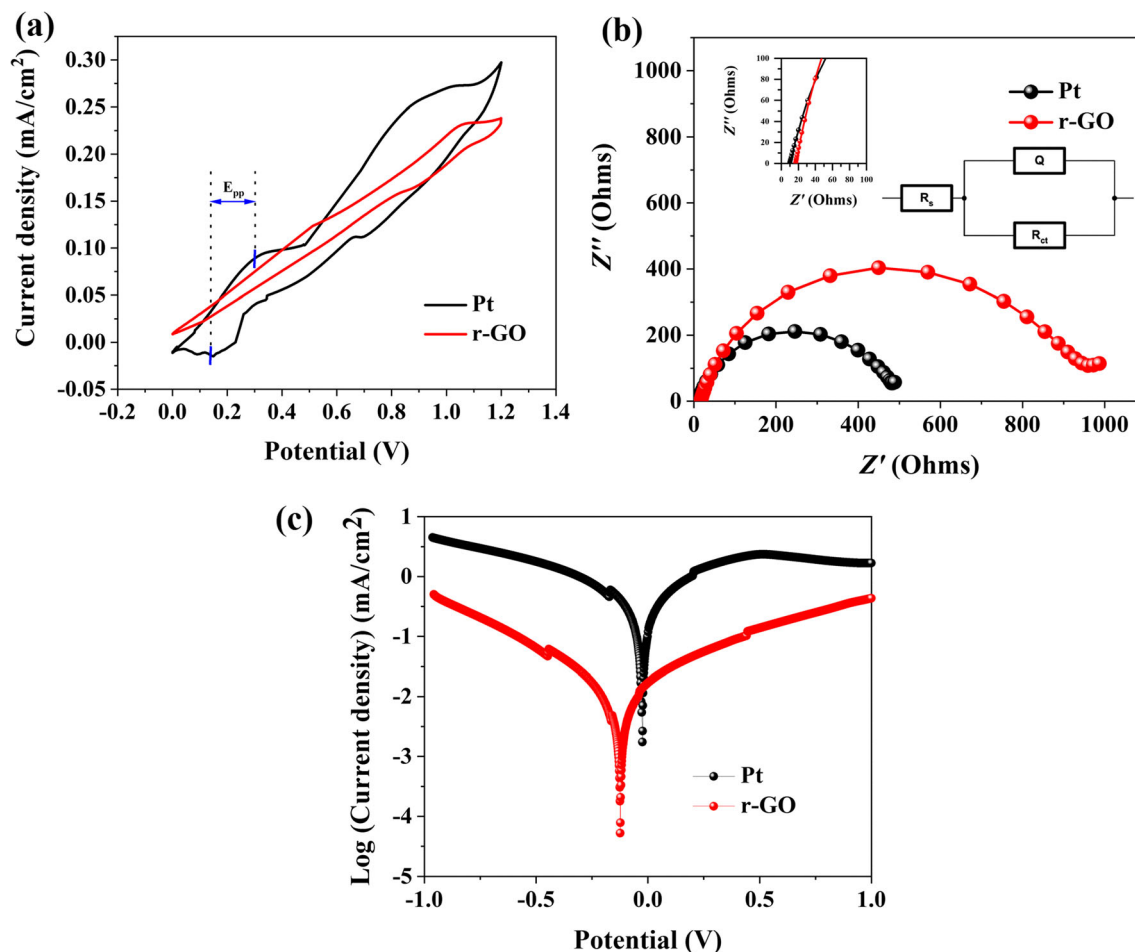


Fig. 10 a CV, b EIS and c Tafel plots of Pt and r-GO CEs

equivalent circuit, the semicircle represents the charge transfer resistance (R_{ct}) at the interface of the CE/electrolyte and the series resistance (R_s) represented by the intercept in high frequency on the real axis, where catalytic activity of CEs was represented by R_{ct} [73]. From the Nyquist plot and equivalent circuit of Pt and r-GO CEs, it is noticeable that the Pt's R_s (9.83 Ω) is lower than r-GO's (16.73 Ω), which can be due to Pt's superior electrical conductivity. Furthermore, the R_{ct} is in the order of r-GO (959 Ω) > Pt (481.5 Ω), showing the effective transfer of charge between surfaces of I_3^- and Pt CE.

To examine the interfacial charge transfer behaviour of CE/electrolyte, the Tafel polarization curves were analysed using the symmetric cells. Tafel polarization curves of Pt and r-GO CEs are represented in Fig. 10c. Exchange current density (J_0) is inversely proportional to R_{ct} ; therefore, a good CE should have lower R_{ct} which produces higher J_0 . J_0 can be estimated from the tangent line intersection of the polarization curve and the linear segment extension to the zero bias [74, 75]. J_{lim} relies on the Γ/I_3^- redox pair diffusion coefficient. Pt exhibits a higher J_{lim} relative to r-GO from the Tafel graph. A lower

Table 2 Photovoltaic parameters obtained from J - V curves

Code	Materials	V_{OC} (V)	J_{SC} (mA cm ⁻²)	FF %	PCE %	R_{ct} (Ω)
Device 1	TiO ₂ /CaBa dye/40% TBAI/r-GO	0.37	3.9	41	0.59	3889
Device 2	2% Ag-TiO ₂ /CaBa dye/40% TBAI/r-GO	0.49	4.09	38	0.77	4938
Device 3	4% Ag-TiO ₂ /CaBa dye/40% TBAI/r-GO	0.5	4.54	47	1.06	7187
Device 4	6% Ag-TiO ₂ /CaBa dye/40% TBAI/r-GO	0.49	4.2	38	0.8	5904
Device 5	4% Ag-TiO ₂ /CaBa dye/40% TBAI/Pt	0.59	5.43	52	1.7	7656
Device 6	4% Ag-TiO ₂ /CaBa dye/40% TBAI/Pt	0.64	6.61	55	2.37	9678

Table 3 Photovoltaic parameters device with different materials obtained from J - V curves

Materials (anode/dye/electrolyte/CE)	V_{OC}	J_{SC} (mA cm ⁻²)	FF %	PCE %	Synthesis method (anode/cathode)	Ref.
TiO ₂ /CaBa/polymer/r-GO	0.37	3.9	41	0.59	Modified sol-gel method/one-pot chemical exfoliation method	This work
2% Ag-TiO ₂ /CaBa/polymer/r-GO	0.49	4.09	38	0.77	Modified sol-gel method/one-pot chemical exfoliation method	This work
4% Ag-TiO ₂ /CaBa/polymer/r-GO	0.5	4.54	47	1.06	Modified sol-gel method/one-pot chemical exfoliation method	This work
6% Ag-TiO ₂ /CaBa/polymer/r-GO	0.49	4.2	38	0.8	Modified sol-gel method/one-pot chemical exfoliation method	This work
4% Ag-TiO ₂ /CaBa/polymer/Pt	0.59	5.43	52	1.7	Modified sol-gel method	This work
4% Ag-TiO ₂ /CaBa/polymer/Pt	0.64	6.61	55	2.37	Modified sol-gel method	This work
TiO ₂ /N719/liquid/Pt	0.69	13.25	55	5.05	Hydrothermal	[18]
Ag _{0.10} -TiO ₂ /N719/liquid/Pt	0.67	17.2	56	6.44	Hydrothermal	[18]
TiO ₂ /N719/liquid/Pt	0.66	7.34	56	2.75	Chemical reduction	[21]
Ag _{0.1 M} -TiO ₂ /N719/liquid/Pt	0.75	12.29	61	5.66	Chemical reduction	[21]
TiO ₂ (P25)/N719/liquid/Pt	0.64	16.62	51	5.55	Commercial	[19]
Ag@TiO ₂ core-shell/N719/liquid/Pt	0.65	11.3	49	3.64	Chemical reduction	[19]
P25:Ag@TiO ₂ = 70:30 wt%/N719/liquid/Pt	0.64	18.22	52	6.06	Physical mixture	[19]
TiO ₂ (P25)/N719/liquid/Pt	0.76	7.48	58	3.35	Commercial	[78]
UV-1.3% Ag-TiO ₂ /N719/liquid/Pt	0.8	8.36	56	3.85	Photochemical reduction	[78]
Glucose-1.3% Ag-TiO ₂ /N719/liquid/Pt	0.8	10.72	52	4.54	Chemical reduction	[78]
Syzygium-1.3% Ag-TiO ₂ /N719/liquid/Pt	0.79	11.8	54	5.12	Chemical reduction	[78]
TiO ₂ /N719/liquid/r-GO	0.75	12.9	49	4.86	Thermal reduction	[62]
TiO ₂ /N719/liquid/Pt	0.74	13.2	54	5.24	Thermal reduction	[62]
TiO ₂ /N719/liquid/r-GO	0.69	15.57	51	5.57	Hydrothermal reduction	[27]
TiO ₂ /N719/liquid/Pt	0.71	16.21	66	7.58	Hydrothermal reduction	[27]
TiO ₂ /N719/liquid/r-GO	0.72	9.22	63	4.16	Photothermal reduction	[79]
TiO ₂ /N719/liquid/Pt	0.7	9.94	68	4.72	Photothermal reduction	[79]
TiO ₂ /N719/liquid/r-GO	0.55	10.68	58	3.44	Hydrothermal reduction	[69]
TiO ₂ /N719/liquid/Pt	0.61	13.14	72	5.78	Hydrothermal reduction	[69]

J_{lim} of r-GO value shows that r-GO's electrocatalytic activity is weak. The J_0 values also display a pattern close to the J_{lim} values, where r-GO showed less J_0 than Pt. A higher J_0 suggests that Pt has high electrocatalytic activity to convert triiodide to iodide, whereas a higher J_{lim} implies strong electrolyte interaction and improved diffusion inside the CE [76, 77].

Photovoltaic performance

The photovoltaic performance of DSSCs under standard AM 1.5 illumination is summarized in Table 2. Figure 10a depicts the current density (J) versus potential (V) plots of different fabricated cells. It was found that Ag-doped TiO₂ nanoparticles showed higher solar conversion efficiency (η) and photocurrent density (J_{SC}) than the bare TiO₂ nanoparticles. Among different Ag-doped TiO₂, 4% Ag-TiO₂ showed the best photovoltaic properties due to their small size, which implies that a large number of dye molecules could be adsorbed. Greater absorption of visible light may enhance the use of sunlight. Nevertheless, the Ag-TiO₂ nanoparticles display an open-

circuit voltage (V_{OC}) higher than the TiO₂ nanoparticles. Also compared to r-GO CE-based DSSC, Pt CE-based DSSC displayed higher efficiency. This lower efficiency was mainly due to the less purity of r-GO. As shown by FT-Raman experiments, the r-GO sample has some residual oxygen-containing functional groups after reduction. Over the course of the photochemical process, the presence of these functional groups will greatly influence the electron transfer kinetics of CEs. In particular, the redox potential and charge transfer resistance will be altered, which can greatly affect the FF, J_{SC} and η . This is reinforced by the higher R_{ct} value of r-GO relative to Pt, found in CE EIS measurements (Fig. 10b). The photovoltaic parameters obtained in our work and in the previous studies are summarized in Table 3.

EIS analysis of DSSCs

The EIS spectra of DSSCs are shown in Fig. 11b, and their equivalent circuit is shown in the inset of Fig. 11b. A typical DSSC EIS spectrum consists of three semicircles. Details on

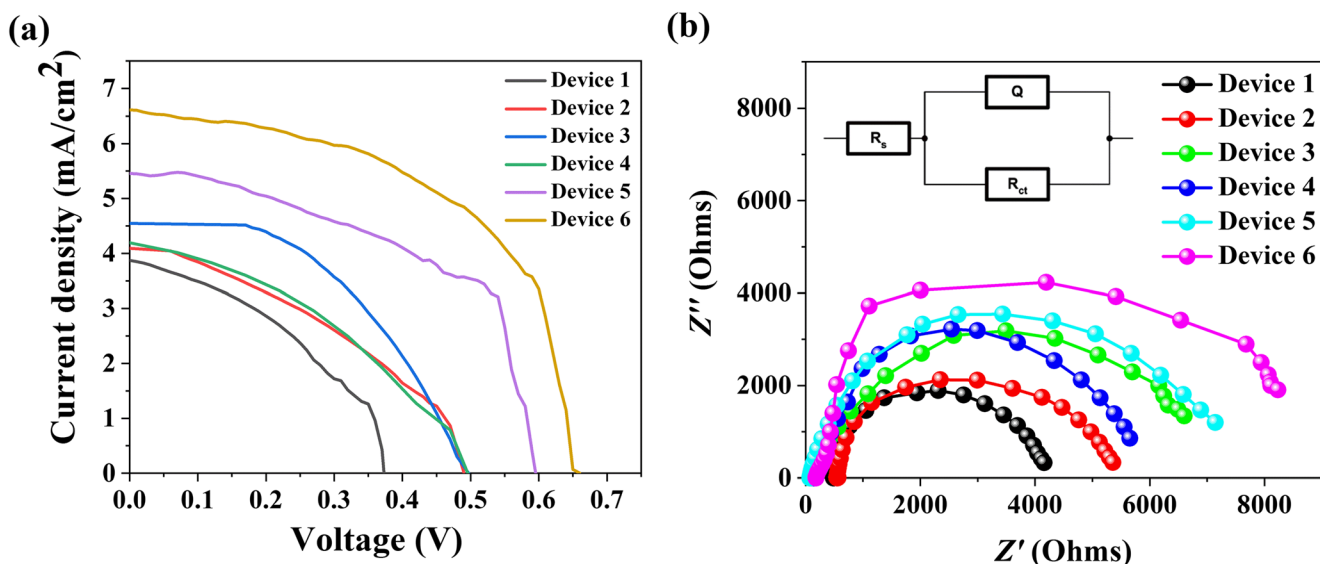


Fig. 11 **a** Current–potential characteristic of the DSSCs under AM 1.5 illumination. **b** EIS spectra of DSSCs

the charge transfer resistance at the CE can be obtained at high frequency, whereas at moderate frequency, electron transport in the photoanode and the back reaction at the interface of photoanode and electrolyte could be obtained. In addition,

diffusion of redox mediator in electrolyte was evaluated using a low-frequency semicircle [80, 81]. Just one semicircle was found in our case. This is because this semicircle occupies and obstructs our ability to view the other two smaller semicircles.

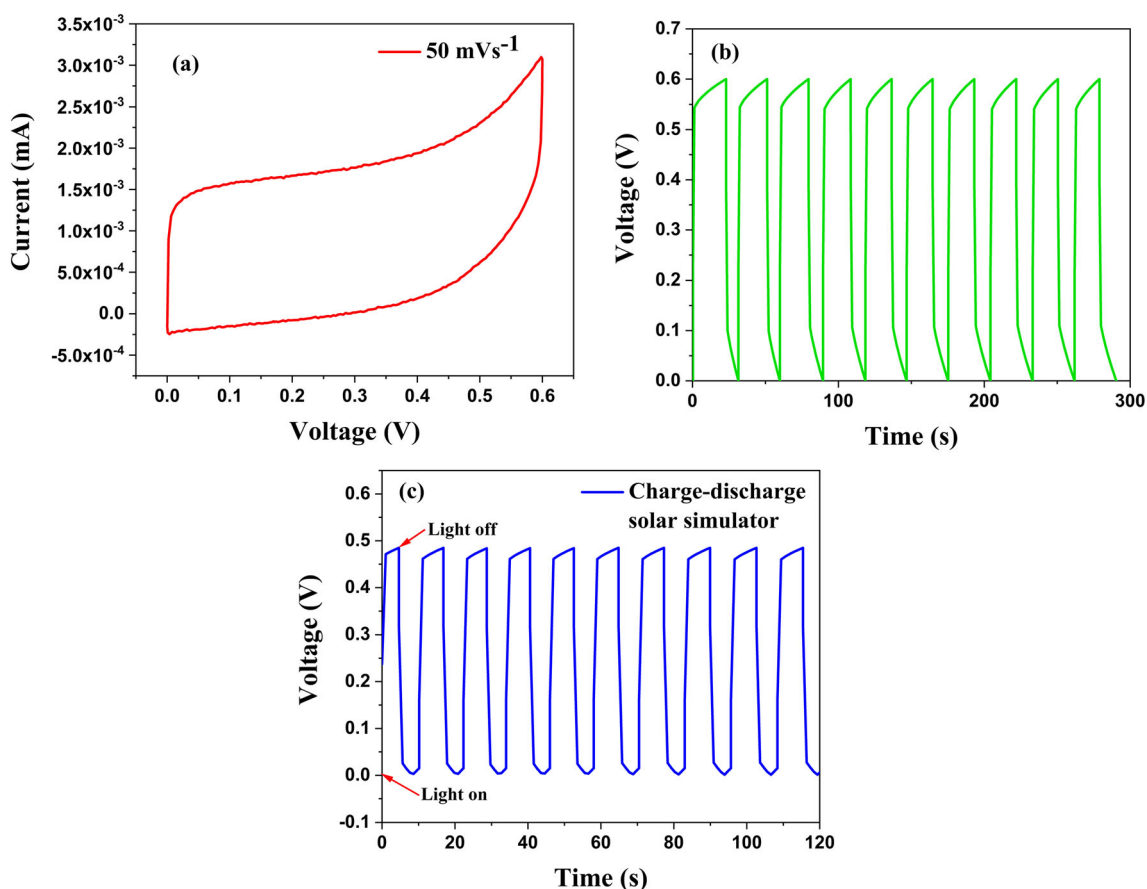


Fig. 12 Electrochemical characterization of SC and DSSC-SC device. **a** Cyclic voltammogram of SC. **b** Charge–discharge curve of SC with constant current density 0.4 mA cm^{-2} . **c** Charge–discharge profiles of an

integrated device which was charged using AM 1.5 illumination and then discharged at a constant current density of 0.4 mA cm^{-2}

Interface resistance of working electrode is directly proportional to the diameter of this semicircle. Low interface resistance leads to a higher recombination rate of charges and results in a lower current density [82, 83]. From Fig. 11b, we can clearly observe that interface resistance follows the order of device 1 < device 2 < device 3 < device 4 < device 5 < device 6 which is in good agreement with current density results listed in Table 2. R_{ct} values obtained using equivalent circuit are displayed in Table 2. R_{ct} is at its highest value of 9678 Ω for device 6 and at its lowest value of 3889 Ω for device 1 which corresponds to the highest and lowest J_{SC} , respectively.

Performance of SC and DSSC-SC-integrated device

Cyclic voltammetry and charge/discharge tests are used to characterize an integrated device. Figure 12a depicts the CV curves of SC which were made from r-GO films as electrodes and 40% TBAI as electrolyte at a potential range of 0 to 0.6 V and under a sweep rate of 50 mV s⁻¹. There are two categories in SC, i.e. a pseudo-capacitor and an electric double-layer capacitor. The CV curve displayed a rectangular shape without current peaks, indicating that the r-GO electrode possesses electrical double layer capacitance [84]. Accordingly, Fig. 12b depicts the charge/discharge at a constant current density of 0.4 mA cm⁻². The discharge time of SC was observed to be about 8.43 s, and the specific capacitance of the device was calculated to be 1.72 Fg⁻¹. Figure 12c depicts the photocharge and discharge of the integrated device. Here, AM 1.5 illumination was used for photocharge and discharge was made with the constant current density of 0.4 mA cm⁻². During photocharging, the voltage increased to 0.485 V, which was slightly lower than V_{OC} in the photoelectric conversion measurement due to electric power lost in the external circuit [85]. The discharge time and specific capacitance of the integrated device were calculated to be 5.23 s and 1.327 Fg⁻¹, respectively.

Conclusion

In summary, we synthesized a novel carbazole-based dye with a carbazole-donating unit and acid group as an acceptor unit and confirmed using IR, NMR and mass spectroscopy. TiO₂ and Ag-doped TiO₂ were synthesized using a modified sol-gel method and characterized by XRD and TEM analysis. Different concentrations of TBAI in PVA-PVP blend polymer electrolytes were prepared, and their conductivity was studied. Among different concentrations, 40% TBAI electrolyte showed the highest conductivity of 1.76 mS cm⁻¹. r-GO was synthesized by a one-pot synthesis method and confirmed using XRD and FT-Raman. DSSCs were fabricated using 40% TBAI electrolyte (due to its high conductivity), bare TiO₂ and 2%, 4% and 6% Ag-doped TiO₂ as anode and r-GO as CE. Among them,

device 3 showed the highest efficiency of 1.06%. Due to its high efficiency among r-GO CE-based DSSCs, this device was used to develop a DSSC-SC-integrated device. The integrated device was tested via photocharging using AM 1.5 illumination and discharging at constant current density. From the results obtained, we conclude that synthesized dye can be used as sensitizer in DSSC and fabricated device successfully converts solar energy to electrical energy which simultaneously stores electrical energy in SC. Further for comparison, device 5 and device 6 were fabricated which have Pt as CE. Device 5 and device 6 displayed the highest efficiency of 1.7% and 2.37%, respectively, compared to r-GO-based devices which are mainly due to high catalytic activity of Pt compared to that of r-GO. The r-GO-based DSSC's lower performance was found to be due to a higher resistance to charge transfer and relatively lower electrocatalytic activity relative to the Pt-based CE. In order to decrease the resistance to charge transfer and increase cell performance, more optimization in the reaction condition is important. The r-GO preparation defined in this paper is environmentally safe, lower cost and scalable. The r-GO obtained is found to be appropriate for DSSC counter electrode applications, and further process optimization is likely to enhance its efficiency to equal that of traditional DSSCs based on Pt.

Abbreviations CV, Cyclic voltammetry; DSSC, Dye-sensitized solar cell; SC, Supercapacitor; TTIP, Titanium tetraisopropoxide; XRD, X-ray diffraction

Supplementary Information The online version contains supplementary material available at <https://doi.org/10.1007/s10008-021-04920-2>.

Funding Open access funding provided by Manipal Academy of Higher Education, Manipal.

Open Access This article is licensed under a Creative Commons Attribution 4.0 International License, which permits use, sharing, adaptation, distribution and reproduction in any medium or format, as long as you give appropriate credit to the original author(s) and the source, provide a link to the Creative Commons licence, and indicate if changes were made. The images or other third party material in this article are included in the article's Creative Commons licence, unless indicated otherwise in a credit line to the material. If material is not included in the article's Creative Commons licence and your intended use is not permitted by statutory regulation or exceeds the permitted use, you will need to obtain permission directly from the copyright holder. To view a copy of this licence, visit <http://creativecommons.org/licenses/by/4.0/>.

References

1. Hemavathi B, Jayadev V, Pradhan SC, Gokul G, Jagadish K, Chandrashekar GK, Ramamurthy PC, Pai RK, Narayanan Unni KN, Ahipa TN, Soman S, Geetha Balakrishna R (2018) Aggregation induced light harvesting of molecularly engineered D-A-II-A carbazole dyes for dye-sensitized solar cells. Sol Energy 174:1085–1096. <https://doi.org/10.1016/j.solener.2018.09.073>

- Han L, Liu J, Liu Y, Cui Y (2019) Novel D-A- π -A type benzocarbazole sensitizers for dye sensitized solar cells. *J Mol Struct* 1180:651–658. <https://doi.org/10.1016/j.molstruc.2018.12.052>
- Kumar D, Wong KT (2017) Organic dianchor dyes for dye-sensitized solar cells. *Mater Today Energy* 5:243–279. <https://doi.org/10.1016/j.mtener.2017.05.007>
- Ji JM, Zhou H, Kim HK (2018) Rational design criteria for D- π -A structured organic and porphyrin sensitizers for highly efficient dye-sensitized solar cells. *J Mater Chem A* 6(30):14518–14545. <https://doi.org/10.1039/c8ta02281j>
- Han L, Islam A, Chen H, Malapaka C, Chiranjeevi B, Zhang S, Yang X, Yanagida M (2012) High-efficiency dye-sensitized solar cell with a novel co-adsorbent. *Energy Environ Sci* 5(3):6057–6060. <https://doi.org/10.1039/c2ee03418b>
- Kang SH, Jeong MJ, Eom YK, Choi IT, Kwon SM, Yoo Y, Kim J, Kwon J, Park JH, Kim HK (2017) Porphyrin sensitizers with donor structural engineering for superior performance dye-sensitized solar cells and tandem solar cells for water splitting applications. *Adv Energy Mater* 7(7):1–10. <https://doi.org/10.1002/aenm.201602117>
- Humphry-Baker R, Rothlisberger U, Nazeeruddin MK et al (2014) Dye-sensitized solar cells with 13% efficiency achieved through the molecular engineering of porphyrin sensitizers. *Nat Chem* 6(3):242–247. <https://doi.org/10.1038/nchem.1861>
- Mishra A, Fischer MKR, Büuerle P (2009) Metal-free organic dyes for dye-sensitized solar cells: from structure: property relationships to design rules. *Angew Chem Int Ed* 48(14):2474–2499. <https://doi.org/10.1002/anie.200804709>
- Ji JM, Kim SH, Zhou H, Kim CH, Kim HK (2019) D- π -A structured porphyrins with extended auxiliary π -spacers for highly efficient dye-sensitized solar cells. *ACS Appl Mater Interfaces* 11(27):24067–24077. <https://doi.org/10.1021/acsami.9b05510>
- Naik P, Elmorsy MR, Su R, Babu DD, el-Shafei A, Adhikari AV (2017) New carbazole based metal-free organic dyes with D-II-A-II-A architecture for DSSCs: synthesis, theoretical and cell performance studies. *Sol Energy* 153:600–610. <https://doi.org/10.1016/j.solener.2017.05.088>
- Han ML, Zhu YZ, Liu S, Liu QL, Ye D, Wang B, Zheng JY (2018) The improved photovoltaic performance of phenothiazine-dithienopyrrole based dyes with auxiliary acceptors. *J Power Sources* 387:117–125. <https://doi.org/10.1016/j.jpowsour.2018.03.059>
- Lima J, Andrade L, Pereira A et al (2017) Styryl and phenylethynyl based coumarin chromophores for dye sensitized solar cells. *J Photochem Photobiol A Chem* 353:564–569. <https://doi.org/10.1016/j.jphotochem.2017.12.018>
- Ohta N, Awasthi K, Okoshi K, Manseki K, Miura H, Inoue Y, Nakamura K, Kono H, Diao EWG (2016) Stark spectroscopy of absorption and emission of indoline sensitizers: a correlation with the performance of photovoltaic cells. *J Phys Chem C* 120(46):26206–26216. <https://doi.org/10.1021/acs.jpcc.6b08531>
- Chiykowski VA, Lam B, Du C, Berlinguette CP (2017) Comparative analysis of triarylamine and phenothiazine sensitizer donor units in dye-sensitized solar cells. *Chem Commun* 53(15):2367–2370. <https://doi.org/10.1039/c6cc09178d>
- Naik P, Su R, Elmorsy MR, el-Shafei A, Adhikari AV (2018) New carbazole based dyes as effective co-sensitizers for DSSCs sensitized with ruthenium (II) complex (NCSU-10). *J Energy Chem* 27(2):351–360. <https://doi.org/10.1016/j.jechem.2017.12.013>
- Patil D, Jadhav M, Avhad K, Chowdhury TH, Islam A, Bedja I, Sekar N (2018) A new class of triphenylamine-based novel sensitizers for DSSCs: a comparative study of three different anchoring groups. *New J Chem* 42(14):11555–11564. <https://doi.org/10.1039/c8nj01029c>
- Suresh T, Chitumalla RK, Hai NT, Jang J, Lee TJ, Kim JH (2016) Impact of neutral and anion anchoring groups on the photovoltaic performance of triphenylamine sensitizers for dye-sensitized solar cells. *RSC Adv* 6(32):26559–26567. <https://doi.org/10.1039/c6ra00636a>
- Dong YX, Wang XL, Jin EM, Jeong SM, Jin B, Lee SH (2019) One-step hydrothermal synthesis of Ag decorated TiO₂ nanoparticles for dye-sensitized solar cell application. *Renew Energy* 135:1207–1212. <https://doi.org/10.1016/j.renene.2018.12.062>
- Chang H, Chen CH, Kao MJ, Hsiao HH (2014) Effect of core-shell Ag@TiO₂ volume ratio on characteristics of TiO₂-based DSSCs. *J Nanomater* 2014:1–8. <https://doi.org/10.1155/2014/264108>
- Gupta AK, Srivastava P, Bahadur L (2016) Improved performance of Ag-doped TiO₂ synthesized by modified sol-gel method as photoanode of dye-sensitized solar cell. *Appl Phys A Mater Sci Process* 122(8):1–13. <https://doi.org/10.1007/s00339-016-0241-2>
- Wu WY, Hsu CF, Wu MJ, Chen CN, Huang JJ (2017) Ag-TiO₂ composite photoelectrode for dye-sensitized solar cell. *Appl Phys A Mater Sci Process* 123(5):1–8. <https://doi.org/10.1007/s00339-017-0963-9>
- Su'ait MS, Rahman MYA, Ahmad A (2015) Review on polymer electrolyte in dye-sensitized solar cells (DSSCs). *Sol Energy* 115:452–470. <https://doi.org/10.1016/j.solener.2015.02.043>
- Farhana NK, Ramesh S, Ramesh K (2019) Efficiency enhancement of dye-sensitized solar cell based gel polymer electrolytes using poly(vinyl butyral-co-vinyl alcohol-co-vinyl acetate)/tetrapropylammonium iodide. *Mater Sci Semicond Process* 91:414–421. <https://doi.org/10.1016/j.mssp.2018.12.007>
- Ng HM, Ramesh S, Ramesh K (2015) Exploration on the P(VP-co-VAc) copolymer based gel polymer electrolytes doped with quaternary ammonium iodide salt for DSSC applications: electrochemical behaviors and photovoltaic performances. *Org Electron* 22:132–139. <https://doi.org/10.1016/j.orgel.2015.03.020>
- Wu J, Lan Z, Lin J, Huang M, Huang Y, Fan L, Luo G, Lin Y, Xie Y, Wei Y (2017) Counter electrodes in dye-sensitized solar cells. *Chem Soc Rev* 46(19):5975–6023. <https://doi.org/10.1039/c6cs00752j>
- Huang C, Li C, Shi G (2012) Graphene based catalysts. *Energy Environ Sci* 5(10):8848–8868. <https://doi.org/10.1039/c2ee22238h>
- Kannan AG, Zhao J, Jo SG, Kang YS, Kim DW (2014) Nitrogen and sulfur co-doped graphene counter electrodes with synergistically enhanced performance for dye-sensitized solar cells. *J Mater Chem A* 2(31):12232–12239. <https://doi.org/10.1039/c4ta01927j>
- Gao Z, Wang L, Chang J, Liu X, Wu D, Xu F, Guo Y, Jiang K (2016) Nitrogen doped porous graphene as counter electrode for efficient dye sensitized solar cell. *Electrochim Acta* 188:441–449. <https://doi.org/10.1016/j.electacta.2015.12.008>
- Yun S, Qin Y, Uhl AR, Vlachopoulos N, Yin M, Li D, Han X, Hagfeldt A (2018) New-generation integrated devices based on dye-sensitized and perovskite solar cells. *Energy Environ Sci* 11(3):476–526. <https://doi.org/10.1039/c7ee03165c>
- Seery MK, George R, Floris P, Pillai SC (2007) Silver doped titanium dioxide nanomaterials for enhanced visible light photocatalysis. *J Photochem Photobiol A Chem* 189(2-3):258–263. <https://doi.org/10.1016/j.jphotochem.2007.02.010>
- Gebregziabher GG, Asemahegne AS, Ayele DW, Dhakshnamoorthy M, Kumar A (2019) One-step synthesis and characterization of reduced graphene oxide using chemical exfoliation method. *Mater Today Chem* 12:233–239. <https://doi.org/10.1016/j.mtchem.2019.02.003>

32. Pei K, Wu Y, Islam A, Zhang Q, Han L, Tian H, Zhu W (2013) Constructing high-efficiency D-A- π -A-featured solar cell sensitizers: a promising building block of 2,3-diphenylquinoxaline for antiaggregation and photostability. *ACS Appl Mater Interfaces* 5(11):4986–4995. <https://doi.org/10.1021/am400754d>
33. Lu X, Jia X, Wang ZS, Zhou G (2013) X-shaped organic dyes with a quinoxaline bridge for use in dye-sensitized solar cells. *J Mater Chem A* 1(34):9697–9706. <https://doi.org/10.1039/c3ta11398a>
34. Li SL, Jiang KJ, Shao KF, Yang LM (2006) Novel organic dyes for efficient dye-sensitized solar cells. *Chem Commun* 2(26):2792–2794. <https://doi.org/10.1039/b603706b>
35. Yang H, Yen Y, Hsu Y et al (2010) Organic dyes incorporating the dithieno[3,2-b:2',3'-d]thiophene moiety for efficient dye-sensitized solar cells. *Org Lett* 12(1):2008–2011. <https://doi.org/10.1021/ol902327p>
36. Pannipara M, Asiri AM, Alamry KA, Arshad MN, el-Daly SA (2015) Synthesis, spectral behaviour and photophysics of donor-acceptor kind of chalcones: excited state intramolecular charge transfer and fluorescence quenching studies. *Spectrochim Acta A Mol Biomol Spectrosc* 136:1893–1902. <https://doi.org/10.1016/j.saa.2014.10.105>
37. Al-Sehemi AG, Pannipara M, Kalam A, Asiri AM (2016) A combined experimental and computational investigation on spectroscopic and photophysical properties of a coumarinyl chalcone. *J Fluoresc* 26(4):1357–1365. <https://doi.org/10.1007/s10895-016-1823-2>
38. Landis RF, Yazdani M, Creran B, Yu X, Nandwana V, Cooke G, Rotello VM (2014) Solvatochromic probes for detecting hydrogen-bond-donating solvents. *Chem Commun* 50(35):4579–4581. <https://doi.org/10.1039/c4cc00805g>
39. Lokhande PKM, Sonigara KK, Jadhav MM, Patil DS, Soni SS, Sekar N (2019) Multi-dentate carbazole based Schiff base dyes with chlorovinylene group in spacer for dye-sensitized solar cells: a combined theoretical and experimental study. *ChemistrySelect* 4(14):4044–4056. <https://doi.org/10.1002/slct.201803940>
40. Salimi Beni A, Zarandi M, Hosseinzadeh B, Najafi Chermahini A (2018) Density functional theory study of carbazole dyes: potential application of carbazole dyes in dye-sensitized solar cells. *J Mol Struct* 1164:155–163. <https://doi.org/10.1016/j.molstruc.2018.02.094>
41. Santos LM, Machado WA, França MD, Borges KA, Paniago RM, Patrocínio AOT, Machado AEH (2015) Structural characterization of Ag-doped TiO₂ with enhanced photocatalytic activity. *RSC Adv* 5(125):103752–103759. <https://doi.org/10.1039/c5ra22647c>
42. Wang F, Zhang S, Li C, Liu J, He S, Zhao Y, Yan H, Wei M, Evans DG, Duan X (2014) Catalytic behavior of supported Ru nanoparticles on the (101) and (001) facets of anatase TiO₂. *RSC Adv* 4(21):10834–10840. <https://doi.org/10.1039/c3ra47076h>
43. Ren R, Wen Z, Cui S, Hou Y, Guo X, Chen J (2015) Controllable synthesis and tunable photocatalytic properties of Ti³⁺-doped TiO₂. *Sci Rep* 5(1):1–11. <https://doi.org/10.1038/srep10714>
44. Albiter E, Valenzuela MA, Alfaro S, Valverde-Aguilar G, Martínez-Pallares FM (2015) Photocatalytic deposition of Ag nanoparticles on TiO₂: metal precursor effect on the structural and photoactivity properties. *J Saudi Chem Soc* 19(5):563–573. <https://doi.org/10.1016/j.jscs.2015.05.009>
45. Suwarnkar MB, Dhabbe RS, Kadam AN, Garadkar KM (2014) Enhanced photocatalytic activity of Ag doped TiO₂ nanoparticles synthesized by a microwave assisted method. *Ceram Int* 40(4):5489–5496. <https://doi.org/10.1016/j.ceramint.2013.10.137>
46. Agyeman DA, Song K, Kang SH, Jo MR, Cho E, Kang YM (2015) An improved catalytic effect of nitrogen-doped TiO₂ nanofibers for rechargeable Li-O₂ batteries; the role of oxidation states and vacancies on the surface. *J Mater Chem A* 3(45):22557–22563. <https://doi.org/10.1039/c5ta05426e>
47. Wang GF, Li MG, Gao YC, Fang B (2004) Amperometric sensor used for determination of thiocyanate with a silver nanoparticles modified electrode. *Sensors* 4(9):147–155. <https://doi.org/10.3390/s40900147>
48. Chang G, Zhang J, Oyama M, Hirao K (2005) Silver-nanoparticle-attached indium tin oxide surfaces fabricated by a seed-mediated growth approach. *J Phys Chem B* 109(3):1204–1209. <https://doi.org/10.1021/jp046652h>
49. Katsiaounis S, Panidi J, Koutselas I, Topoglidis E (2020) Fully reversible electrically induced photochromic-like behaviour of Ag:TiO₂ thin films. *Coatings* 10(2):130. <https://doi.org/10.3390/coatings10020130>
50. Baran E, Yazici B (2016) Effect of different nano-structured Ag doped TiO₂-NTs fabricated by electrodeposition on the electrocatalytic hydrogen production. *Int J Hydrog Energy* 41(4):2498–2511. <https://doi.org/10.1016/j.ijhydene.2015.12.028>
51. Ran H, Fan J, Zhang X, Mao J, Shao G (2018) Enhanced performance of dye-sensitized solar cells based on Au-TiO₂ and Ag-TiO₂ plasmonic hybrid nanocomposites. *Appl Surf Sci* 430:415–423. <https://doi.org/10.1016/j.apsusc.2017.07.107>
52. Sakthivel T, Kumar KA, Senthilselvan J, Jagannathan K (2018) Effect of Ni dopant in TiO₂ matrix on its interfacial charge transportation and efficiency of DSSCs. *J Mater Sci Mater Electron* 29(3):2228–2235. <https://doi.org/10.1007/s10854-017-8137-2>
53. Feng X, Shankar K, Paulose M, Grimes CA (2009) Tantalum-doped titanium dioxide nanowire arrays for dye-sensitized solar cells with high open-circuit voltage. *Angew Chem Int Ed* 48(43):8095–8098. <https://doi.org/10.1002/anie.200903114>
54. Shaikh SF, Mane RS, Joo OS (2015) La₂O₃-encapsulated SnO₂ nanocrystallite-based photoanodes for enhanced DSSCs performance. *Dalton Trans* 44(7):3075–3081. <https://doi.org/10.1039/c4dt03564j>
55. Zhang H, Lv Y, Guo Y, Tao X, Yang C, Zhou X (2018) Fully-air processed Al-doped TiO₂ nanorods perovskite solar cell using commercial available carbon instead of hole transport materials and noble metal electrode. *J Mater Sci Mater Electron* 29(5):3759–3766. <https://doi.org/10.1007/s10854-017-8310-7>
56. Bandara TMWJ, Jayasundara WJMJSR, Dissanayake MAKL, Fernando HDNS, Furlani M, Albinsson I, Mellander BE (2014) Quasi solid state polymer electrolyte with binary iodide salts for photo-electrochemical solar cells. *Int J Hydrog Energy* 39(6):2997–3004. <https://doi.org/10.1016/j.ijhydene.2013.05.163>
57. Ravi M, Pavani Y, Kiran Kumar K, Bhavani S, Sharma AK, Narasimha Rao VVR (2011) Studies on electrical and dielectric properties of PVP:KBrO₄ complexed polymer electrolyte films. *Mater Chem Phys* 130(1-2):442–448. <https://doi.org/10.1016/j.matchemphys.2011.07.006>
58. Raghu S, Kilarkaje S, Sanjeev G, Devendrappa H (2013) Electron beam induced modifications in conductivity and dielectric property of polymer electrolyte film. *Radiat Meas* 53–54:56–64. <https://doi.org/10.1016/j.radmeas.2013.03.017>
59. Ramesh S, Liew CW (2013) Dielectric and FTIR studies on blending of [xPMMA-(1-X)PVC] with LiTFSI. *Meas J Int Meas Confed* 46(5):1650–1656. <https://doi.org/10.1016/j.measurement.2013.01.003>
60. Tan CY, Farhana NK, Saidi NM, Ramesh S, Ramesh K (2018) Conductivity, dielectric studies and structural properties of P(VA-co-PE) and its application in dye sensitized solar cell. *Org Electron* 56:116–124. <https://doi.org/10.1016/j.orgel.2018.02.007>
61. Zhang R, Zhang B, Sun S (2015) Preparation of high-quality graphene with a large-size by sonication-free liquid-phase

- exfoliation of graphite with a new mechanism. *RSC Adv* 5(56):44783–44791. <https://doi.org/10.1039/c5ra04480d>
62. Senthilkumar R, Raj SM, Ramakrishnan S, Kumaresan D, Kothurkar NK (2018) Thermally reduced graphene oxide as a counter electrode material for dye-sensitized solar cells. *J Nanosci Nanotechnol* 19(4):2158–2165. <https://doi.org/10.1166/jnn.2019.16360>
 63. Johra FT, Lee JW, Jung WG (2014) Facile and safe graphene preparation on solution based platform. *J Ind Eng Chem* 20(5):2883–2887. <https://doi.org/10.1016/j.jiec.2013.11.022>
 64. Muhammad Hafiz S, Ritikos R, Whitcher TJ, Md. Razib N, Bien DCS, Chanlek N, Nakajima H, Saisopa T, Songsiriritthigul P, Huang NM, Rahman SA (2014) A practical carbon dioxide gas sensor using room-temperature hydrogen plasma reduced graphene oxide. *Sensors Actuators B Chem* 193:692–700. <https://doi.org/10.1016/j.snb.2013.12.017>
 65. Rajaura RS, Srivastava S, Sharma V, Sharma PK, Lal C, Singh M, Palsania HS, Vijay YK (2016) Role of interlayer spacing and functional group on the hydrogen storage properties of graphene oxide and reduced graphene oxide. *Int J Hydrog Energy* 41(22):9454–9461. <https://doi.org/10.1016/j.ijhydene.2016.04.115>
 66. Gui CX, Wang QQ, Hao SM, Qu J, Huang PP, Cao CY, Song WG, Yu ZZ (2014) Sandwichlike magnesium silicate/reduced graphene oxide nanocomposite for enhanced Pb^{2+} and methylene blue adsorption. *ACS Appl Mater Interfaces* 6(16):14653–14659. <https://doi.org/10.1021/am503997e>
 67. Wang R, Wang Y, Xu C, Sun J, Gao L (2013) Facile one-step hydrazine-assisted solvothermal synthesis of nitrogen-doped reduced graphene oxide: reduction effect and mechanisms. *RSC Adv* 3(4):1194–1200. <https://doi.org/10.1039/c2ra21825a>
 68. Gurulakshmi M, Meenakshamma A, Susmitha K, Charanadhar N, Srikanth VVSS, Narendra Babu S, Venkata Subbaiah YP, Venkateswarlu K, Raghavender M (2019) A transparent and Pt-free all-carbon nanocomposite counter electrode catalyst for efficient dye sensitized solar cells. *Sol Energy* 193:568–575. <https://doi.org/10.1016/j.solener.2019.09.081>
 69. Sarkar A, Bera S, Chakraborty AK (2020) CoNi₂S₄-reduced graphene oxide nanohybrid: an excellent counter electrode for Pt-free DSSC. *Sol Energy* 208:139–149. <https://doi.org/10.1016/j.solener.2020.07.075>
 70. Mary CI, Senthilkumar M, Manobalaji G, Babu SM (2020) Surface-treated Cu₂ZnSnS₄ nanoflakes as Pt-free inexpensive and effective counter electrode in DSSC. *J Mater Sci Mater Electron* 31(20):18164–18174. <https://doi.org/10.1007/s10854-020-04365-9>
 71. Zhang C, Deng L, Zhang P et al (2017) Hydrothermal synthesis of NiS₂ cubes with high performance as counter electrodes in dye-sensitized solar cells. *Int J Electrochem Sci* 12:4610–4618. <https://doi.org/10.20964/2017.05.100>
 72. Silambarasan K, Archana J, Athithya S, Harish S, Sankar Ganesh R, Navaneethan M, Ponnusamy S, Muthamizhchelvan C, Hara K, Hayakawa Y (2020) Hierarchical NiO@NiS@graphene nanocomposite as a sustainable counter electrode for Pt free dye-sensitized solar cell. *Appl Surf Sci* 501:144010. <https://doi.org/10.1016/j.apsusc.2019.144010>
 73. Li S, Min H, Xu F, Tong L, Chen J, Zhu C, Sun L (2016) All electrochemical fabrication of MoS₂/graphene counter electrodes for efficient dye-sensitized solar cells. *RSC Adv* 6(41):34546–34552. <https://doi.org/10.1039/c6ra02494g>
 74. Chen M, Shao LL (2016) Review on the recent progress of carbon counter electrodes for dye-sensitized solar cells. *Chem Eng J* 304:629–645. <https://doi.org/10.1016/j.cej.2016.07.001>
 75. Hwang I, Yong K (2015) Counter electrodes for quantum-dot-sensitized solar cells. *ChemElectroChem* 2(5):634–653. <https://doi.org/10.1002/celec.201402405>
 76. Mustafa MN, Shafie S, Zainal Z, Sulaiman Y (2017) A novel poly(3,4-ethylenedioxythiophene)-graphene oxide/titanium dioxide composites counter electrode for dye-sensitized solar cell. *J Nanomater* 2017:1–9. <https://doi.org/10.1155/2017/4045672>
 77. Younas M, Gondal MA, Dastageer MA, Baig U (2019) Fabrication of cost effective and efficient dye sensitized solar cells with WO₃-TiO₂ nanocomposites as photoanode and MWCNT as Pt-free counter electrode. *Ceram Int* 45(1):936–947. <https://doi.org/10.1016/j.ceramint.2018.09.269>
 78. Tian Z, Wang L, Jia L, Li Q, Song Q, Su S, Yang H (2013) A novel biomass coated Ag-TiO₂ composite as a photoanode for enhanced photocurrent in dye-sensitized solar cells. *RSC Adv* 3(18):6369–6376. <https://doi.org/10.1039/c3ra40195b>
 79. Yeh MH, Lin LY, Chang LY, Leu YA, Cheng WY, Lin JJ, Ho KC (2014) Dye-sensitized solar cells with reduced graphene oxide as the counter electrode prepared by a green photothermal reduction process. *ChemPhysChem* 15(6):1175–1181. <https://doi.org/10.1002/cphc.201301128>
 80. Chiappara C, Figà V, Di Marco G et al (2016) Investigation of recovery mechanisms in dye sensitized solar cells. *Sol Energy* 127:56–66. <https://doi.org/10.1016/j.solener.2016.01.010>
 81. Bramhankar TS, Pawar SS, Shaikh JS, Gunge VC, Beedri NI, Baviskar PK, Pathan HM, Patil PS, Kambale RC, Pawar RS (2020) Effect of nickel–zinc co-doped TiO₂ blocking layer on performance of DSSCs. *J Alloys Compd* 817:152810. <https://doi.org/10.1016/j.jallcom.2019.152810>
 82. Mehmood U, Ahmad SHA, Khan AUH, Qaiser AA (2018) Co-sensitization of graphene/TiO₂ nanocomposite thin films with ruthenizer and metal free organic photosensitizers for improving the power conversion efficiency of dye-sensitized solar cells (DSSCs). *Sol Energy* 170:47–55. <https://doi.org/10.1016/j.solener.2018.05.051>
 83. Tan CY, Omar FS, Saidi NM, Farhana NK, Ramesh S, Ramesh K (2019) Optimization of poly(vinyl alcohol-co-ethylene)-based gel polymer electrolyte containing nickel phosphate nanoparticles for dye-sensitized solar cell application. *Sol Energy* 178:231–240. <https://doi.org/10.1016/j.solener.2018.12.043>
 84. Yang Z, Li L, Luo Y, He R, Qiu L, Lin H, Peng H (2013) An integrated device for both photoelectric conversion and energy storage based on free-standing and aligned carbon nanotube film. *J Mater Chem A* 1(3):954–958. <https://doi.org/10.1039/c2ta00113f>
 85. Dong P, Rodrigues MTF, Zhang J, Borges RS, Kalaga K, Reddy ALM, Silva GG, Ajayan PM, Lou J (2017) A flexible solar cell/supercapacitor integrated energy device. *Nano Energy* 42:181–186. <https://doi.org/10.1016/j.nanoen.2017.10.035>

Publisher's note Springer Nature remains neutral with regard to jurisdictional claims in published maps and institutional affiliations.